NOAA Technical Memorandum GLERL-148

FINAL REPORT: COMPUTATIONAL MODELING OF BALLAST WATER TANKS TO IMPROVE UNDERSTANDING AND MAXIMIZE EFFECTIVENESS OF MANAGEMENT PRACTICES AND TREATMENT MECHANISMS. PHASE II -- EXTENSION OF LABORATORY STUDY

Peter A. Chang III[1], Wesley Wilson[1], Jason Carneal[1], Paisan Atsavapranee[1], Stephan Verosto[1], David F. Reid[2], and Philip T. Jenkins[3]

[1]Naval Surface Warfare Center-Carderock Division, West Bethesda, MD
[2]NOAA, Great Lakes Environmental Research Laboratory, Ann Arbor, MI
[3]Philip T. Jenkins and Associates, LTD, Fonthill, ON, Canada

September 2009

UNITED STATES
DEPARTMENT OF COMMERCE

Gary Locke
Secretary

NATIONAL OCEANIC AND
ATMOSPHERIC ADMINISTRATION

Jane Lubchenco
Under Secretary for Oceans & Atmosphere
NOAA Administrator

NOTICE

Mention of a commercial company or product does not constitute an endorsement by the NOAA. Use of information from this publication concerning proprietary products or the tests of such products for publicity or advertising purposes is not authorized. This is GLERL Contribution No. 1532.

This publication is available as a PDF file and can be downloaded from GLERL's web site: www.glerl.noaa.gov. Hard copies can be requested from GLERL Information Services, 4840 S. State Rd., Ann Arbor, MI 48108. pubs.glerl@noaa.gov.

NOAA's Mission – To understand and predict changes in Earth's environment and conserve and manage coastal and marine resources to meet our nation's economic, social, and environmental needs

NOAA's Mission Goals:

- Protect, restore and manage the use of coastal and ocean resources through an ecosystem approach to management.
- Understand climate variability and change to enhance society's ability to plan and respond.
- Serve society's needs for weather and water information.
- Support the Nation's commerce with information for safe, efficient, and environmentally sound transportation.
- Provide critical support for NOAA's Mission.

Suggested Citation: Chang, P.A., III, W. Wilson, J. Carneal, P. Atsavaprance, S. Verosto, D.F. Reid, and P. Jenkins. Final Report: Computational Modeling of Ballast Water Tanks to Improve Understanding and Maximize Effectiveness of Management Practices and Treatment Mechanisms, Phase II -- Extension of Laboratory Study. NOAA Technical Memorandum GLERL-148. NOAA Great Lakes Environmental Research Laboratory, Ann Arbor, MI and NSWCCD-50-TR-2009/028, Naval Surface Warfare Center Carderock Division, West Bethesda, MD, 78 pp. (2009).
ftp://ftp.glerl.noaa.gov/publications/tech_reports/glerl-148/tm-148.pdf

CONTENTS

FIGURES

TABLES

ERRATA

Technical errors identified in this document will be documented and corrected here. This section will be updated as appropriate in the on-line version of this Technical Memorandum.

(09-2009) Pages 50 and 51: Table 7 and Figure 32 both erroneously label the hopper side tank (HST) and the wing tank (WT) as “HT” and “TT” (topside tank) respectively.

NOMENCLATURE

B	tank beam, m
H	tank height, m
L	tank length, m
Q	flow rate, m^3/sec
T	temperature, ^oC
v	volume fraction
Vo	tank volume, m^3
ρ	density, kg/m^3
σ	standard deviation

ABBREVIATIONS

BrW	brackish water
BWE	ballast water exchange
CFD	computational fluid dynamics
DBT	double bottom tank
EE	exchange efficiency
FPS	frames per second
FW	fresh water
FS	full scale
GLERL	Great Lakes Environmental Research Laboratory
HST	hopper side tank
LIF	laser-induced fluorescence
MH	manhole
NOAA	National Oceanic and Atmospheric Administration
NSWCCD	Naval Surface Warfare Center - Carderock Division
SW	saltwater
SWEVF	saltwater effluent volume fraction (volume fraction of SW in the effluent at the tank outlet pipe)
SWVF	saltwater volume fraction (at locations within the tank)
TVE	tank volumes exchanged
VF	volume fraction
V&V	verification and validation

Final Report: Computational Modeling of Ballast Water Tanks to Improve Understanding and Maximize Effectiveness of Management Practices and Treatment Mechanisms, Phase II -- Extension of Laboratory Study September 2009

P.A. Chang III, W. Wilson, J. Carneal, P. Atsavapranee, S. Verosto,
D.F. Reid, and P.T. Jenkins

EXECUTIVE SUMMARY

INTRODUCTION

Mid-ocean ballast water exchange (BWE) is presently the primary management practice with widespread acceptance for reducing or preventing the spread of nonindigenous aquatic species via ballast water. Attempts to determine the efficiency of BWE via on-board experiments have generally produced inconsistent and unreliable results. Such experiments are labor intensive and difficult to run, so reproducibility is difficult to demonstrate for the same ship and tank structure. In addition, on-board experiments involving flow-through exchange generally relied on measurements taken at the overflow outlet of the tank, which may not represent the actual volume mixture that remains in the ballast tank. Given the complex structural nature of ballast tanks and the difficulty of obtaining direct experimental verification from inside ballast tanks, development of a computer-based model of the flow and mixing dynamics in ballast tanks during flow-through exchange can provide several advantages over on-board experimental approaches, and can also help interpret such experimental results. The NOAA Ballast Water Technology Demonstration Program provided funding for GLERL and NSWCCD to design and build a 1/3-scale model BWE facility and to develop a computational model for predicting BWE efficacy. In Phase I of this effort, documented in Wilson et al.[1] a 1/3-scale physical model facility was built at NSWCCD.

In this report the (physical) scale-model experimental setup and measurement techniques used in Phases I and II of this project are described. Then, the results and the two-fluid physics that were observed during the entire 3-TVE are shown. In the CFD section the methodology is described followed by comparisons of the CFD predictions with the measured quantities from the

[1] Wesley Wilson, Peter A. Chang, Stephan Verosto, Paisan Atsavapranee, David Reid, and Phil Jenkins. Computational and experimental analysis of ballast water exchange. In Maritime Environmental Engineering Symposium (MEETS 2006), Crystal City, VA, 2006. ASNE.

physical scale-model experiments. Additionally, full-scale simulations are documented and an Appendix shows the uncertainty analysis.

EXPERIMENTAL METHODOLOGY

In Phase I of this program, 1/3-scale model experiments were performed at a single flow rate and maximum density difference (freshwater ballast vs. influent seawater) for a single tank-volume-exchange (TVE). Also in Phase I the detailed CFD studies necessary for maximizing the accuracy while minimizing the run times of the computational model were performed. For Phase II, the capacity of the facility was increased to allow experiments over three-TVE and three different exchange conditions were tested: 1) 3-TVE BWE with saltwater (salinity = 35) being pumped at 4.1 ℓ/sec (65 gpm, equal to 1,012 gpm equivalent flow rate at full scale) into a ballast tank filled with freshwater; 2) saltwater (salinity = 35) being pumped into a ballast tank filled with brackish water (salinity = 20) at the same flow rate; and 3) saltwater (salinity = 35) being pumped into a ballast tank filled with brackish water (salinity = 20) at 6.9 ℓ/sec (110 gpm, equal to 1,700 gpm equivalent flow-rate at full scale).

Laser-induced fluorescence (LIF) was used to capture planar images of flow and mixing in the up to four regions of interest during each experimental run. LIF images were analyzed to calculate volume fraction (the relative amount of saltwater at each pixel location) and mixedness (the amount of mixing at each pixel or averaged over each data plane) within the imaged regions for comparison against CFD model simulations of the same conditions. In addition, a fluorimeter was positioned in a horizontal section of the model's outlet piping to record the two-fluid composition of the outflow over time. This mimics the location where samples used to calculate exchange efficiency (EE) have been taken during on-board flow-through exchange experiments.

EXPERIMENTAL RESULTS (SCALE MODEL BWE EXPERIMENTS)

The raw LIF images showed turbulent structures, areas of hideout, and the level of mixing within the planar areas imaged. Examples are provided and the features represented are discussed, along with a qualitative assessment of how changing the density and flow rate changed the observed flow and mixing dynamics. Graphs of the mixedness function and the saltwater volume fraction (SWVF) at each LIF image plane in the experimental tank versus time (TVE), and the saltwater effluent volume fraction (SWEVF) measured by the fluorimeter in the outlet pipe for each experimental condition are presented and interpreted. The LIF data show that a decrease in density difference between

the original ballast water and the exchanging saltwater allows increased mixing throughout the ballast tank. Increases in inlet flow rate also increase the amount of mixing throughout the tank. Increases in density difference between the original fluid and the incoming exchange fluid can lead to increasing hideout of original fluid if the incoming flow does not have sufficient momentum to scour the pockets of trapped fluid from the tank tops. The effluent time histories suggest that exchanging fluids with large differences in density approaches the behavior of plug flow, whereas fluids of closer density approach a pure mixing condition as density difference is decreased and flow rate is increased.

COMPUTATIONAL METHODOLOGY

CFD simulations were performed using the commercial viscous flow solver, *Fluent* (developed by Ansys, Inc.). The setup of the code parameters and model grid structure is described and discussed.

ONE-THIRD SCALE CFD RESULTS

Graphical comparisons of the 1/3-scale model experimental data and CFD-predicted values for each of the three test conditions over the full 3-TVE exchange, are presented and discussed.

SWEVF and EE: EE is an integral measure of the volume of the two fluids within the tank at a given time and therefore is a reflection of the volume of each of the two fluids that exit the tank. CFD values of EE are computed directly by a spatial integration of the SWVF over all grid cells within the CFD tank model, whereas experimental EE values are computed indirectly as the difference between the volume of SW entering the tank and the volume that has exited the tank, the latter based on the fluorimeter data (SWEVF) collected in the outlet pipe. It is shown that the CFD-predicted EE match the expected physical trends: as mixing increases, due to either an increase in flow rate or decrease in density difference, the EE at the end of three tank volumes increases. The computational predictions fall within the 95% uncertainty intervals for the EE computed from experimental data. However, we suggest that SWEVF as a basis for estimating EE can be problematic as it does not take into account the spatial inhomogeneities that may exist within the tank during BWE, and can under-predict the EE early on and over-predict EE during the latter stages of BWE. For the case where the density differences are small, SWEVF can start to approach EE in the mid- to later stages of an exchange.

SWVF: The saltwater volume fraction (SWVF) averaged over the camera data planes from each experiment (Conditions 1-3) over the complete 3-TVE exchange and that predicted by CFD are presented graphically and compared and interpreted, as are the CFD-predicted vs. experimental Mixedness parameter. The comparisons show that the CFD can predict the volume fraction (SWVF) quite well implying that the mass movement of the two fluids throughout the tank is well-predicted.

The CFD comparisons of mixedness are on the whole, quite good, particularly for conditions 1 and 2, which involve less mixing, but for condition 3, the mixing is under-predicted. This appears to be due to the highly energetic mixing caused by overturning gravity waves and turbulence in the bellmouth bay.

Since the 1/3-scale tank is limited to two bay lengths, we suggest that the relative amount of energy available for mixing and scouring in the two adjacent bays of the 1/3-scale model is much higher than it will be across the entire full-scale tank with 10 bays. In a full-scale tank the far downstream energy levels should approach quiescent, and mixing should approach zero, no matter what the flow rate and density difference.

FULL-SCALE CFD SIMULATIONS

Full-scale CFD simulations were performed for a complete ballast tank from a typical 35,000 dwt handysize bulk carrier. The complete tank consists of interconnected double bottom tank (DBT), hopper side tank (HST), and wing tank (WT), each segmented into ten bays (27 m total length). The WT is connected to the HST via two 20.3 cm (8 in) diameter connection pipes. The incoming fluid is pumped into the DBT via a single inlet bellmouth. There are two exits that were modeled as flush with the tank top directly above the two connection pipes through which the overflow exits the tank during BWE. The tank floor openings and stiffeners were modeled based on tank drawings provided by Fednav International. The total volume of the tank (with longitudinal stringers) is 705 m^3 (186,250 gals). The inflow rate was 11.4 m^3/min (3000 gpm), meaning that a one tank volume exchange takes 62 min (real time). The tank is initially full of freshwater and exchanged (flow-through) with mid-ocean saltwater giving a density difference equivalent to a salinity difference of 35.

Some previous applications of CFD to ballast tank flow were performed without some of the structural detail, especially the longitudinal stringers along the bottom and sometimes the top of ballast tanks to for strength. The inclusion of the structural detail such as stringers has a significant impact on the computational resources and time required to perform such simulations. In

order to investigate the influence of stringers on the simulation outcomes, two separate representations (grids) were developed for the full-scale tank, one with all of the tank structure and one that omits the longitudinal stringers.

The inclusion of longitudinal stringers in the computational geometry had a profound impact on the two-fluid mixing in the tank and on the EE. Without stringers the two fluids in the inlet bay are completely mixed, with highly mixed fluid regions thereafter quickly dispersing throughout the tank. With the stringers the flow is much less mixed, with almost pure SW forming overturning waves in the vicinity of the bellmouth and moving along the tank bottom. We believe the most important effect is in the stringers ability to restrain mixing in the transverse direction. With this limitation, the amount of mixing is dramatically reduced and the SWEVF and EE time histories approach that for plug flow filling.

In the full-scale CFD simulations BWE did not reach the required 95% EE for the tank configuration and combination used here, but the difference at 3-TVE is not statistically different than 95%. It appears that the primary cause for loss of EE is trappage of water in the tank tops. However, neither the CFD nor the experimental model included the quarter-round vent holes at the top of the tank bays in the actual ballast tank. These would allow a small flow of water across the tank top toward the exit pipes, and should act to decrease possibility of water trappage, and possibly increase the calculated EE.

SUMMARY AND CONCLUSIONS

The combined experimental and computational approaches provide new insights into the physics of BWE. Significant findings are:

1. The predicted values of EE fall within the experimental error bands, showing that the CFD model has been validated.
2. Comparisons between CFD and experimental SWEVF and mixedness data within the tank show that the CFD predicts these quantities reasonably well. One shortcoming is the under-prediction of the amount of mixing with a higher flow rate and lower density difference.
3. The exclusion of the quarter-round vent holes at the top of the tank bays might have led to a slight lowering of the calculated EE. However, due to size of a full-scale tank, the kinetic energy at the interface and the pressure forces pushing the flow through these holes would be very small.
4. Longitudinal stiffeners (LS) are very effective at decreasing the extent of mixing within the inlet bay. With LS the early exchange approaches plug flow filling. The latter stages of exchange approach the perfect mixing case,

but the maximum EE is reduced by FW hideout in the tank top. This result shows that in a full-scale tank there is insufficient kinetic energy to scour water trapped at the tank top (water hideout).

5. Not including the LS in the CFD model allows nearly homogenous and instantaneous mixing to occur across the entire inlet bay. The EE curve approaches that for perfect mixing, especially near 3-TVE.
6. These simulations indicate that if mixing in the inlet bay can be substantially reduced, AND the quarter-rounds at the tank tops are effective in reducing the water hideout in the tank tops, it may be possible to perform a 95% exchange in significantly less than 3-TVs.

CFD allows examination of a wide range of ballast exchange conditions across any tank architecture. It allows evaluation of the effects of various parameters and small scale tank architecture on the outcomes of exchange. One aspect of ballast water exchange not incorporated into the present model is the effects of ship motion on the exchange process - ballast water exchange must be conducted on the high seas. Additional work on this application of CFD modeling should incorporate equations of motion that account for roll and pitch of a moving vessel.

We conclude that CFD modeling is a very useful approach for investigating and understanding ballast tank flow and that use of CFD model-based calculations of EE can be a practical alternative to on-board experiments. However, appropriate resolution of tank structure and CFD cell grid densities must be allowed for maximum benefit.

APPENDIX A: UNCERTAINTY ANALYSIS

Appendix A provides an analysis of the uncertainty associated with determination of the mixedness parameter and the fluid volume fractions. Based on this analysis, the relative uncertainty in the LIF measurements on which mixedness and volume fractions of fluids are based is approximately 0.66% over the whole field, while for a single pixel measurement the relative uncertainty approaches 9.84%. Our calculations of mixedness and volume fractions of fluids over an entire bay has a very low uncertainty due to the large number of points interrogated simultaneously by the LIF technique. It should be noted that in future studies the linearity of the LIF (CCD) sensor response versus dye concentration should be determined experimentally in order to better estimate the error associated with the assumption of linear response.

Final Report: Computational Modeling of Ballast Water Tanks to Improve Understanding and Maximize Effectiveness of Management Practices and Treatment Mechanisms, Phase II -- Extension of Laboratory Study
September 2009

P.A. Chang III, W. Wilson, J. Carneal, P. Atsavapranee, S. Verosto,
D.F. Reid, and P.T. Jenkins

ABSTRACT

Ballast water exchange (BWE) has been the most common method for reducing the transport and discharge of nonindigenous aquatic species associated with ballast tanks of ships traveling around the world. To reduce the spread of nonindigenous aquatic species, vessels exchange coastal ballast water with mid-ocean seawater, aiming for a minimum of 95% volume replacement. Measuring the exchange efficiency on board operating ships is extremely difficult and subject to large variances. Here we examine the use of computational fluid dynamics (CFD) to model ballast tank water flow and predict the exchange efficiency (EE).

In order to compare and validate the model with experimental data, flow and exchange experiments were performed with a one-third scale four-compartment model of section of a bulk carrier ballast tank that includes two double-bottom and two hopper side compartments. The experiments were run for a full three-tank-volume exchange (3-TVE). In order to mimic the conditions of most concern to the North American Great Lakes, the tank was initially filled with fresh or brackish (equivalent density) water and the incoming (exchanging) fluid was a salt, alcohol, and water mixture adjusted to approximate the density of 35 ppt seawater. Experiments were performed with two density differences and two flow rates that scale to those typically used in ballast water exchange.

Transient, two-fluid CFD simulations were developed for the one-third scale model as well as for a full-scale bulk carrier ballast tank. Data from the four-compartment 1/3-scale CFD model simulations is compared with the experimental data. Comparisons of the data within the tank are quite good. CFD predictions of EE show that the CFD can predict the right trends and falls within the experimental error bands. Two full-scale CFD simulations were run to determine the CFD model's sensitivity to relatively small structures (longitudinal stringers). The results show that these structures are very important to the physics of two-fluid mixing and lead to significant changes in the EE.

We conclude that CFD modeling is a very useful approach to understand ballast tank flow and that use of CFD model-based calculations of EE could be a practical alternative to on-board experiment.

ACKNOWLEDGEMENTS

This Technical Memorandum is the final report by the NOAA Great Lakes Environmental Research Laboratory (Ann Arbor, MI) for a multi-year, multi-institutional research project to investigate the potential use of computer modeling to understand mixing and flow dynamics in commercial ship ballast tanks during flow-through ballast water exchange. The project was funded by the NOAA Ballast Water Technology Demonstration Program (Dorn Carlson, Program Manager).

Fednav International (Montreal, Quebec, Canada) provided detailed ship information and ballast tank blueprints needed for accurate creation of the physical and CFD models.

This document substantially incorporates final project report NSWCCD-50-TR–2009/028 submitted by the Naval Surface Warfare Center – Carderock Division to the NOAA Great Lakes Environmental Research Laboratory in fulfillment of Award #01-3WCA90018.

ADMINISTRATIVE INFORMATION

This was a joint project between the NOAA Great Lakes Environmental Research Laboratory (Ann Arbor, MI) and the Naval Surface Warfare Center, Carderock Division (West Bethesda, MD). It was sponsored by the NOAA Ballast Water Technology Demonstration Program (Dr. Dorn Carlson, Program Manager) and carried out at the Naval Surface Warfare Center — Carderock facilities.

INTRODUCTION

Mid-ocean ballast water exchange (BWE) is presently the primary management practice with widespread acceptance for reducing or preventing the spread of non-indigenous aquatic species via ballast water. BWE is the process whereby coastal ballast water, which contains the unwanted organisms, is flushed from the ballast tanks through the introduction of mid-ocean seawater. One method to achieve this is called flow-through ballast water exchange and is the subject of this research. Flow-through BWE is accomplished by overflowing a filled or partially filled ballast tank by pumping seawater into the tank via the normal ballast intake lines. On most existing ships, seawater enters at the bottom of the tank and displaces and/or dilutes the coastal ballast water. If perfect mixing is assumed, then 3 tank volumes of seawater are necessary to achieve a 95% exchange efficiency (EE).[7] EE is the proportion of the original tank water that is replaced by the influent seawater.

While ballast exchange by itself is not the method of choice in the long-term, it is likely to remain in use until there is both widespread acceptance of specific ballast water biological discharge standards and widespread availability of more effective, technology-based, treatment approaches that meet those standards. The IMO Convention on Ballast Water Management[1] proposed discharge standards and set a very aggressive agenda to establish on-board treatment of all ballast water by 2016, but this schedule is unlikely to be achievable and has already been delayed by a year. No technologies for on-board treatment of ballast water discharge have been verified for routine shipboard use in U.S. waters, although there are a number of systems in various stages of development and IMO approval.[2] Thus it is likely that BWE will continue in the foreseeable future as a (or the) primary ballast water management practice with widespread availability and use. Therefore, it is useful to understand the ballast water exchange process, the flow dynamics inside a ballast tank during exchange, and how tank architectures affect the outcome.

Past attempts to determine the efficiency of BWE via on-board experiments have produced inconsistent and generally unsatisfactory results. Many of the direct on-board experiments conducted in the past suffered from design and/or implementation deficiencies exacerbated by the complex structure, inaccessibility of typical ballast tanks, and the fact that experimentalists did not usually have control of the ship (the test platform). These difficulties limited the experimental design and resolution of sampling to determine exchange effectiveness related to coastal organisms. However, well-planned and controlled experiments by the Smithsonian Environmental Research Center[8] showed

that properly conducted BWE can be highly effective at replacing coastal ballast water with mid-ocean water (88-99% replacement of original water) and flushing out or killing coastal planktonic organisms (80-95% reduction in concentration) across ship types, when conducted according to guidelines and regulations. However, such experiments are labor intensive and difficult to run, so reproducibility is difficult to demonstrate for the same ship and tank structure. In addition, such on-board experiments generally rely on measurements taken at the overflow outlet of the tank and may not represent the volume mixture that remains in the ballast tank. Given the complex structural nature of ballast tanks and the difficulty of obtaining direct experimental verification from inside ballast tanks, development of a computer-based model of the flow and mixing dynamics in ballast tanks can provide several advantages over on-board experimental approaches, and can also help interpret such experimental results.

A successful model, one that has been fully validated and verified, will predict ballast water EE, is portable and can be tailored to different tank types and geometries, different exchange flow rates, and different initial conditions. There is no need to wait for another transoceanic voyage to retest or run a test on the same tank under different conditions. The validated and verified model will provide insight into the flow and mixing dynamics in the inaccessible recesses of a ballast tank, and can thus identify hidden areas of the tank that may contain low fluid velocities (commonly referred to as dead spots), or the occurrence of short-circuiting, where a stream of influent water moves from inlet to outlet by the most direct route, never mixing throughout the tank. Identifying and understanding phenomena such as dead spots and short-circuiting provides the basis for developing approaches and improvements to the overall effectiveness and consistency of the exchange process. A verified model can also be used to test the effects of modifications to internal tank structures and cutouts. A verified fluid flow model can be expanded to incorporate modules to examine the behavior of passive "particles," such as phytoplankton or sediment, and possibly even active particles, such as zooplankton. Such models can help understand why ballast water exchange may not be as efficient for biological exchange as it is for water exchange, and under what conditions this is true, as well as possible solutions. Areas of sediment deposition may also be identified and proposed modifications to tank structures can be tested using computer modeling prior to making any actual modifications to operational tank design, to determine if there are ways to decrease sediment deposition and compaction.

An accurate CFD simulation of BWE must incorporate flows through complicated tank structures that include an inlet bellmouth (the bottom of the inlet pipe is usually flaired, appearing like an inverted funnel, and is called the bellmouth), longitudinal stringers, transverse and longitudinal floors, manholes, limber holes and air vent holes. Longitudinal stringers are the framing found along the tops and bottoms of the tanks. Floors are the vertical partitions that divide the tank into compartments. Manholes are openings in the floors that allow for human access and fluid flow between compartments. Limber holes are the smaller 6-inch diameter circular drain holes between the compartments. Air vents are the very small ($100 - 150\ mm$ full scale radius) half- and quarter-round air vent openings in the top of the tanks to allow passage of air and fluid

along the top of the tank. Drain holes are the very small ($100 - 150$ mm full scale radius) half- and quarter-round openings in the bottom of the tanks to allow drainage of fluid along the bottom of the tank.

Accurate CFD simulations also involve the simulation of two fluids, the initial ballast water and the influent seawater, which, depending on the salinity, may be at different starting densities. Thus, CFD models must successfully model the displacement of one fluid by another, and must simulate the mixing of one fluid into another. CFD efforts have taken a step-by-step approach to solving the problem. The first published efforts were by Holdo, Armstrong and Rose[5] who performed CFD calculations on a double bottom tank with a simplified geometric arrangement, using steady state single-fluid simulations. They showed where in the tank mixing should occur and where the flow is stagnant and would resist being flushed out. Kent and Parsons[6] used two-fluid modeling, performing simulations on J-type ballast tanks with single and dual outlet ports, and hopper side/upper wing tank ballast tanks. However, while useful, their results are limited by use of relatively coarse grids, tank geometries that did not include longitudinal stringers, and the lack of validations with experimental data.

In order to assess the validity of any computational model it is important to validate it against physical experimental data. While it would be ideal to obtain test data during full-scale BWE, such experiments are very expensive and access to the interior ballast tank structure difficult. Although sensors could be placed at various locations throughout the tank, it would be difficult if not impossible to obtain the data resolution necessary for understanding the two-fluid flow and mixing physics within the tank. The NOAA Ballast Water Technology Demonstration Program provided funding for GLERL and NSWCCD to design and build a model-scale BWE facility and to develop a computational model for predicting BWE efficacy. In Phase I of this effort, documented in Wilson et al.,[9] a 1/3-scale model facility was built at NSWCCD. The tank models four bays of a typical bulk-carrier double bottom and side hopper tank and is built to a 1:3 geometric scale. In Phase I the experiments were performed at a flow rate that scales to 1100 gpm full-scale. The most important mixing flows in the vicinity of the bellmouth are scaled such that the ratio of buoyancy to inertial forces (Richardson number) is the same at model- and full-scale. Experiments were performed at a single flow rate and maximum density difference (freshwater ballast vs. influent seawater) for a single tank-volume-exchange (TVE). Also in Phase I the detailed CFD studies necessary for maximizing the accuracy while minimizing the run times of the computational model were performed. These studies included the effects of time-stepping and advective-differencing schemes, turbulence modeling and grid refinement. The shortcoming of Phase I is that it only included the first TVE whereas BWE requirements are based on a three-TVE. While the most energetic mixing events occur in the first TVE, the second and third TVE are important because they lead to the final two-fluid configuration at the end of BWE. The physics of the second- and third-TVE are assumed to be that of tank top scouring, but really are not clearly understood.

In this report the 1/3-scale model experimental setup and measurement techniques used in Phases I and II of this project are described. Then, the results and the two-

fluid physics that occur during the entire three-TVE are shown. In the CFD section the methodology is described followed by comparisons of the CFD predictions with the measured quantities. Additionally, full-scale simulations are documented and finally conclusions and recommendations for follow-on work are made. An appendix shows the uncertainty analysis.

EXPERIMENTAL METHODOLOGY

Scaling

Full-scale bulk carrier ballast tanks are on the order of 10's of meters long, with exchange rates of up to 3000 *gpm*. Obviously it is not possible to build such a large model or obtain such large flow rates and the resulting velocities in a model-scale facility. However, it may be possible to model correctly some of the most important two-fluid mixing events. From earlier work with ships compensated fuel/ballast it was discovered that most of the two-fluid mixing occurs at the inlet jet and inflows through manholes.[4] For stratified shear flows, the Richardson number (the ratio between the buoyancy and inertial forces), is the most important parameter for two-fluid mixing. Low Richardson numbers imply that the buoyancy force is relatively small and a large amount of mixing will occur. As Richardson number increases, the flows become increasingly stable and mixing decreases.[3]

Equating model- and full-scale Richardson numbers for the radial flow from the bellmouth along the tank floor, it is possible to show that the volume inflow rates are related by the 5/2-power of the scale ratio. Using this relationship it is possible to show that the flows between the longitudinal stiffeners and through the manholes are Richardson scaled. The scale ratio of 3 was chosen because it would give a tank with a volume of 1.433 m^3 (378 *gal*), allowing the use of readily available 1.9 m^3 (500 *gal*) supply and waste tanks for the initial one-TVE experiment.

The Reynolds number is the ratio between inertial and viscous forces and may also be an important parameter as it gauges the amount of turbulent activity present. For small Reynolds numbers, the viscous forces dominate and below certain thresholds, dependent upon geometry, the flow will be laminar. As Reynolds numbers increase the inertial forces dominate and the flow is susceptible to small disturbances and becomes turbulent. Turbulent flow is comprised of eddies which will tend to increase the entrainment of one fluid into the other. The Reynolds number of the inflow jet scales as the 3/2-power of the scale ratio. A 1/3-scale model would provide a pipe Reynolds number that was fully turbulent. The Reynolds numbers throughout the tank however, may not be fully turbulent as the velocity magnitude decreases away from the bellmouth jet —though this may occur in the full-scale tanks as well. For full-scale tanks the range of Reynolds numbers between the bellmouth and far reaches of the tanks will be on the order of 10^6 with flows ranging from highly turbulent near the bellmouth jet to laminar in far reaches of the tank. In this model scale tank, the Reynolds number at the bellmouth is much smaller than for full-scale, yet because only four compartments are modeled, the range of Reynolds number found in the tank will be much less. Therefore, at model scale there may be a relatively large amount of turbulent activity in the "downstream" bays that may not occur in full-scale downstream bays. In fact, as the results show, there is a large amount of tank top scouring that takes place at model scale that may not actually take place in a full-scale geometry.

Ballast Water Facility

The test tank, shown in Figure 1, is a 1/3-scale model of four compartments of a bulk carrier ballast tank, including two double bottom (abbreviated as DB1 and DB2) and two hopper side tank (HST1 and HST2) compartments. The tank has features similar to those found in full-scale tanks, including the bellmouth, the longitudinal stringers along the top and bottom of the tank, the transverse and longitudinal floors, manholes, limber holes and the exit pipe. Thus, the test tank contains all the structural features found in full-scale tanks and therefore, would have many of the same types of flow features. The test tank does not have air vent or drain hole openings in the tops and bottoms of the tanks, respectively.

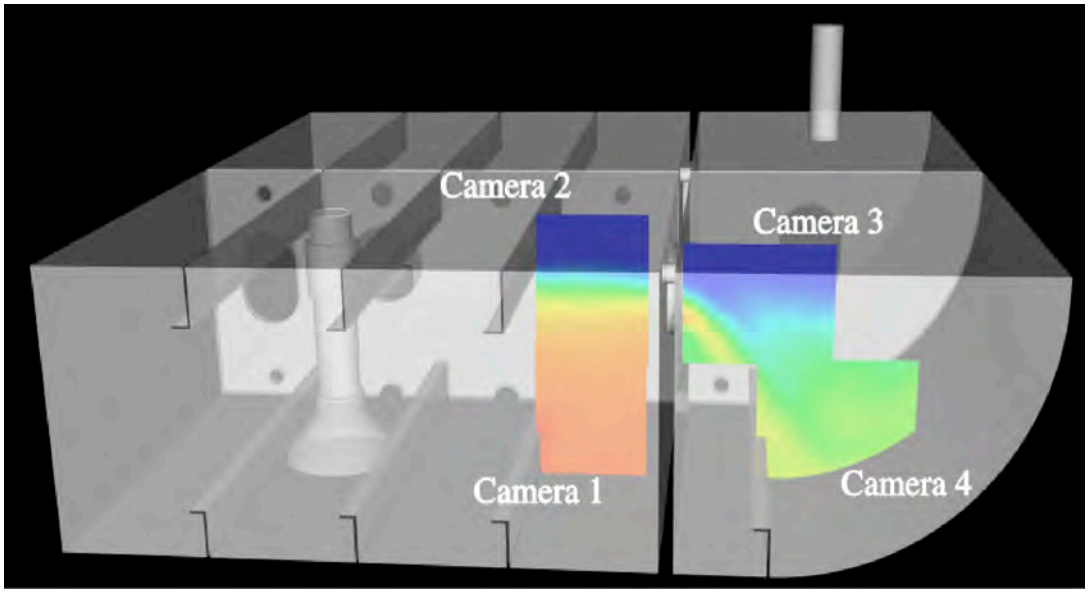

Figure 1. Drawing of test tank and LIF camera planes. The compartment designations are as follows: lower left: DB1, upper left: DB2, lower right: HST1, upper right: HST2.

The test tank was constructed of 1.905 cm (3/4 in) thick acrylic and has a capacity of approximately 1.433 m^3 (378 $gals$). This is the same test tank used for CFD Phase I, which allowed only one-TVE experiments. For Phase II, the capacity of the facility was increased to allow experiments over three-TVE. The modified facility has two 3.8 m^3 (1000 gal) supply tanks, one 1.9 m^3 (500 gal) premix tank, and two 1.9 m^3 (500 gal) waste tanks, providing sufficient capacity for three-TVE experiments. The two 3.8 m^3 (1000 gal) supply tanks supply the 12.6 ℓ/sec (200 gpm) centrifugal pump through 5.08 cm (2 in) tank outlets combined through a (5.08 $cm \times 7.62\ cm \times 5.08\ cm$) (2 $in \times$ 3 $in \times 2\ in$) tee. This unique configuration provides for a more even pump suction head allowing more precise flow control. The pump discharge is regulated by a 7.62 cm (3 in) diaphragm valve. The facility is plumbed primarily with the 7.62 cm (3 in), Schedule

80, PVC pipe with a 6.99 cm (2.75 in) inner diameter, which scales satisfactorily for the actual 20.3 cm (8 in) tank feeder pipes of a full-scale tank.* "Quick" disconnects and flexible hoses allow for relatively easy change outs of plumbing components. A schematic of the test facility is shown in Figure 2. Flow rates are measured using a vortex shedding flowmeter equipped with local indication and $4 - 20$ mA output for data recording. It has an accuracy of $\pm 1\%$ flow and a repeatability of 0.2%.

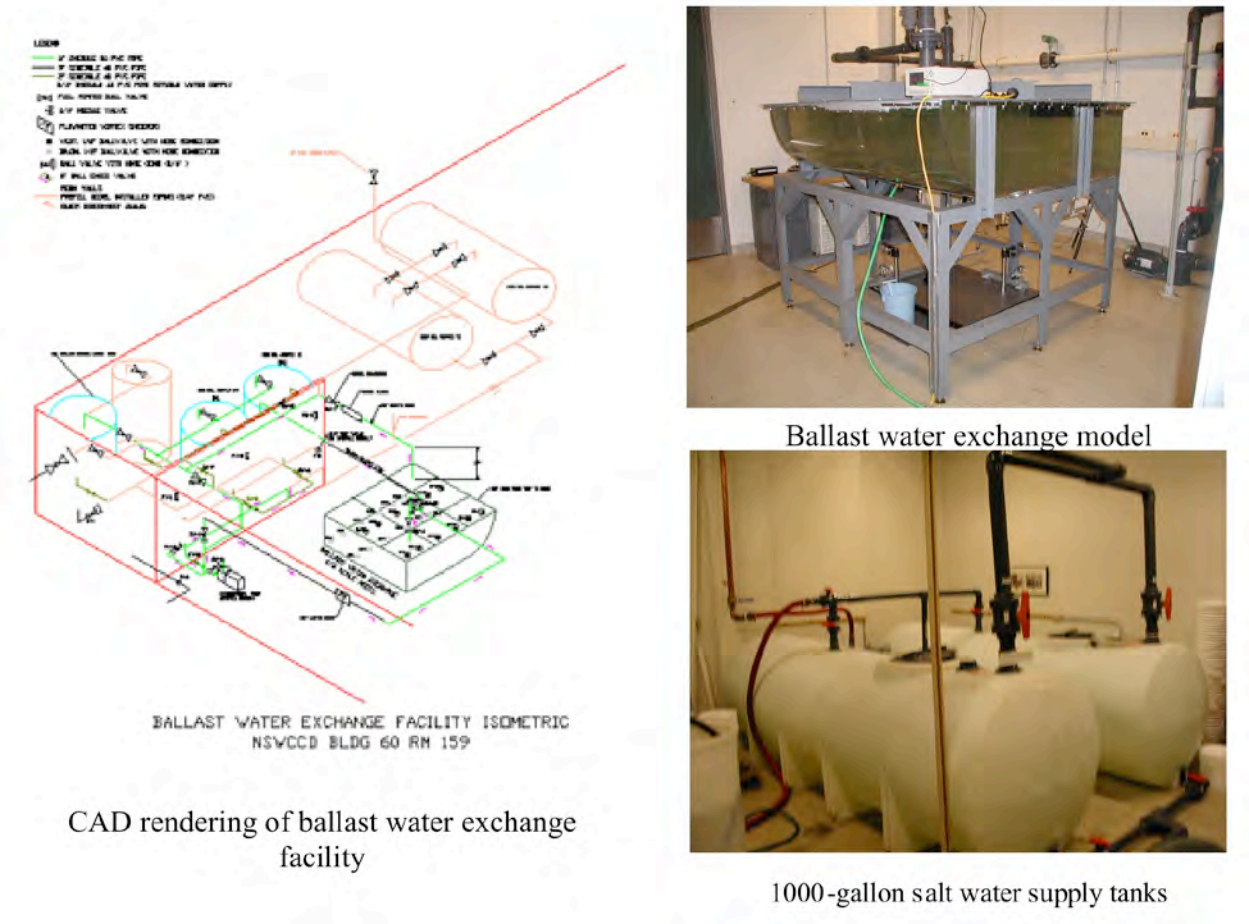

Figure 2. CAD rendering and photographs of the modified ballast water facility at NSWCCD.

Experimental Test Plan and Test Procedure

In order to provide a comprehensive dataset for CFD validation, experiments were performed at a variety of flow rates and conditions as listed in Table 1. The experiments performed during the course of this work were intended to study the dynamics of ballast water exchange between two fluids of varying density in a model scale environment.

*At full scale, the 20.3 cm (8 in) diameter tank feeder pipes are fed by main feeder pipes with a diameter of 30 cm (12 in)

Since the utilization of true ocean water was impractical, a solution of magnesium sulfate ($MgSO_4$) was used to simulate seawater with a density equivalent to salinity = 35 in order to simplify the water preparation procedure and provide a stably stratified fluid interface. In order to match the index of refraction of the $MgSO_4$ solution and provide the desired density differences, ethanol was added to the freshwater that initially filled the tank.

A total of three conditions were tested. Condition 1 simulated a ballast water exchange process with 35 parts-per-thousand (*ppt*) saltwater being into pumped into a tank full of freshwater at a flow rate of 4.1 ℓ/sec (65 *gpm* model scale = 1,012 *gpm* full scale). This is the flow rate used in the Phase I work documented in Wilson et al.[9] Condition 2 simulates a ballast water exchange with salinity = 35 saltwater being pumped into a tank full of salinity = 20 brackish water at the same flow rate. In condition 3, the flow rate was increased to 6.9 ℓ/sec (110 *gpm*) for the saltwater (salinity = 35) to brackish (salinity = 20) water exchange, which corresponds to a full scale flow rate of 1700 *gpm*. The correspondence between the non-dimensional times and the times in seconds are listed in Table 2.

Table 1. Experimental test plan.

Condition	Q (gpm)	TargetΔ ρ	ρ_{MgSO_4}	$\rho_{Ethanol}$	n	Sim'd Exchange
1	65	0.025	1.014	0.989	1.3361	SW to FW
2	65	0.010	1.005	0.995	1.3343	SW to BrW
3	110	0.010	1.005	0.995	1.3343	SW to BrW

Table 2. Correspondence between non-dimensional time, t^*, and dimensional time in *secs*, for the three test conditions.

t^*	Condition		
	1	2	3
0.02	7.0	7.0	3.5
0.05	17.4	17.4	8.7
0.086	30.0	30.0	15.0
0.1	35	35	17
0.2	70	70	35
0.5	174	174	87
1	349	349	174
2	698	698	349
3	1047	1047	523

The waste and supply tanks, supply and waste lines, and the ballast tank model were all cleaned thoroughly prior to experimentation. The 1.9 m^3 (500 *gal*) supply tank

for the alcohol and two 1.9 m^3 (500 gal) waste tanks were filled with water through a 5 μm filter. $MgSO_4$ ("salt") was added to the water in the two waste tanks with the mixers engaged to ensure a homogenous solution. The saltwater tanks were iterated independently to the desired test condition as listed in Table 1 by adding incremental amounts of salt and testing the density and index of refraction between iterations. The saltwater preparation process was repeated for the second 3.8 m^3 (1000 gal) supply tank. Once the 3.8 m^3 (1000 gal) supply tanks were filled with the salt solution, both the fresh- and salt-water were left overnight to de-gas. The next morning, alcohol was added to the freshwater supply tank and iterated to produce the desired density and index of refraction as listed in Table 1. Ice was added to the freshwater supply tank to match the temperature of the saltwater. Sample alcohol and $MgSO_4$ solution iterations from the Condition 1 test are shown in Table 3 and Table 4.

Once the indices of refraction were matched at the desired density difference, Rhodamine-6G dye was added to the freshwater and the tank was thoroughly stirred to ensure proper mixing of the dye. The scale-model ballast tank was then initially filled with dyed freshwater from the 1.9 m^3 (500 gal) supply tank. The saltwater was pumped in recirculation mode until the desired flow rate was obtained and the test was ready to start. To initiate the test, the model valve was opened simultaneously with the closing of the recirculation valve, and the salt solution was introduced into the test tank. Data was collected until three TVE had occurred [approximately 4.3 m^3 (1136 $gals$)]. For the 4.1 ℓ/sec (65 gpm) and 6.9 $liter/sec$ (110 gpm) cases, this translated to approximately 17.5 $mins$ and 10.4 $mins$, respectively. During the course of the data acquisition, the actual flow rate was manually read every thirty seconds to confirm uniform and steady flow during the experiment. After data acquisition was completed, the pump was shut down and the model was drained. The model was then filled with pure salt solution, and dark images were taken of the solution with no dye for data processing purposes. The test procedure was repeated for each condition listed in Table 1.

Table 3. Alcohol solution preparation.

Iter	ρ	n	$T(^oC)$	Alc. Added ($gal.$)
0	1			0
1	0.995			15
2	0.992		14.5	27
3	0.9895		15.0	30
4	0.9915		13.5	30
5	0.9905		13.5	33
6	0.9890	1.3364	14.0	36
7	0.9900	1.3363	14.0	36
8	0.9901	1.3362	14.0	36
9	0.9905	1.3361	14.0	36

Table 4. $MgSO_4$ solution preparation.

Iter	ρ	n	$T(^oC)$	Alc. Added ($gal.$)
0	1.00			0
1	—			175
2	1.014		14.0	250
3	1.017	1.3364	14.5	275
4	1.015	1.3362	14.5	

Measurement Techniques and Experimental Setup

LIF Setup

The LIF experimental setup is shown in Figure 3 and camera plane locations in the test tank are shown in Figure 1. Planar images in the regions of interest were taken with four progressive-scan CCD (charge-coupled device) cameras (Hitachi model #KP-120CL) with a spatial resolution of 1392 pixels × 1040 pixels and a full frame rate of 15 Hz. Cameras 1, 2 and 3 were fitted with 50 mm C-mount lens, and camera 4 was fitted with a 25 mm lens for a larger field of view. Filters were placed on each camera in order to filter out the laser source and record only fluoresced light. Images from all cameras were captured using a data-acquisition computer capable of streaming images from four cameras simultaneously at the full camera frame rate onto a real-time disk array system with a capacity of 625 gigabytes. For system redundancy, images can also be optionally captured to 1.8 gigabytes of RAM.

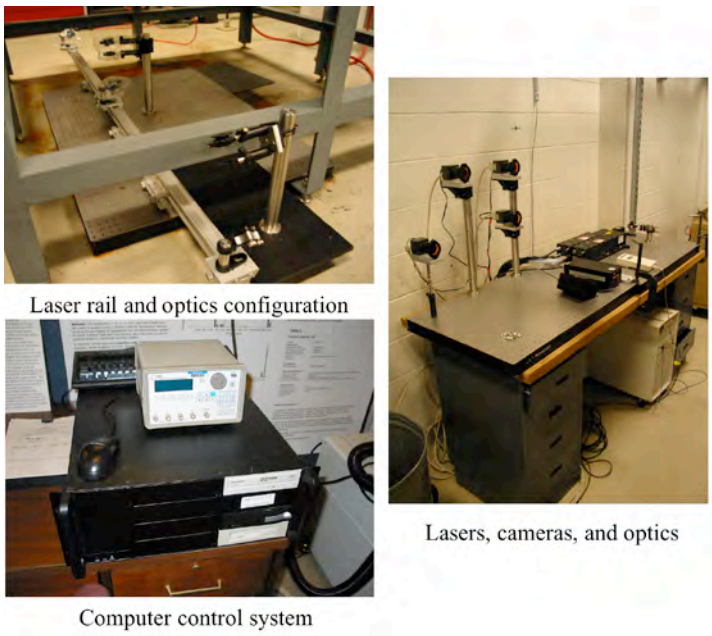

Figure 3. LIF experimental setup.

Illumination of the flow field was provided by a dual-head Nd:YAG laser (Big Sky model #CFR-400), operating at 532 nm. Each head of the pulse laser operates with a maximum optical energy output of 250 mJ per pulse, at a rate of 15 Hz. For our experiments, a single laser head was used since the data collection rate was 15 Hz. This data collection rate was chosen to provide sufficient information on the flow field while allowing timely processing of the collected data.

The output beam from the laser was steered using a series of mirrors so that the laser beams ran parallel to the test tank bottom. The energy of the beams was split into two using a dichroic beamsplitter, and each resulting beam was reflected into a vertical path underneath each measurement region using a mirror. Each beam was then passed through a plano-spherical lens (1000 mm) and a cylindrical lens (25 mm) to create the two laser sheets, illuminating the regions of interest for each camera. The laser sheet illuminating the field of view of cameras 1 and 2 was centered under the measurement region and oriented vertically, and the laser sheet illuminating the fields of view of cameras 3 and 4 was located outboard and oriented at an angle into the curved portion of the model to avoid blockage by the supporting structure. Rhodamine-6G dye was added to the freshwater (initial tank volume) to provide fluoresced light during the experiment. All interrogation regions were placed parallel to the plane of the center of the inlet pipe. Cameras 1 and 2 interrogate the bay upstream of the manhole as shown in Figure 1. Camera 3 interrogates the flow exiting the manhole, and Camera 4 captures the impingement of the jet from the manhole on the curved surface of the ballast water tank.

Fluorimeter Setup and Calibration

The fluorimeter was installed in a horizontal section of the model's outlet piping. It was calibrated in-vivo by inserting various solutions of known dye concentration into the test section. Between measurement points, the test section was rinsed thoroughly with clean water by filling and draining twice. Successive measurements were made to gain calibration curves of both voltage and intensity versus dye concentration. A picture of the fluorimeter setup and the calibration data obtained are shown in Figure 4. The R^2 value of the linear fits ranged from 0.9985 to 0.9987, which demonstrated the linearity of the fluorimeters response.

Conductivity sensor setup and calibration

The conductivity sensors were mounted in compartment DB2 using a support structure as shown in Figure 5. The conductivity sensors were calibrated using mixtures of pure alcohol and pure saltwater solutions encountered during the experiment. The calibration curve for one of the conductivity sensors is shown in Figure 5 (bottom). The conductivity sensors were designed to measure salinity in an ocean environment and therefore had maximum sensitivity in seawater conditions. As expected, the calibration curve in Figure 5 (bottom) shows that the conductivity sensors only respond to the higher range of $MgSO_4$ encountered in this set of experiments and that below a certain concentration threshold, they cannot detect conductivity variations. This means that

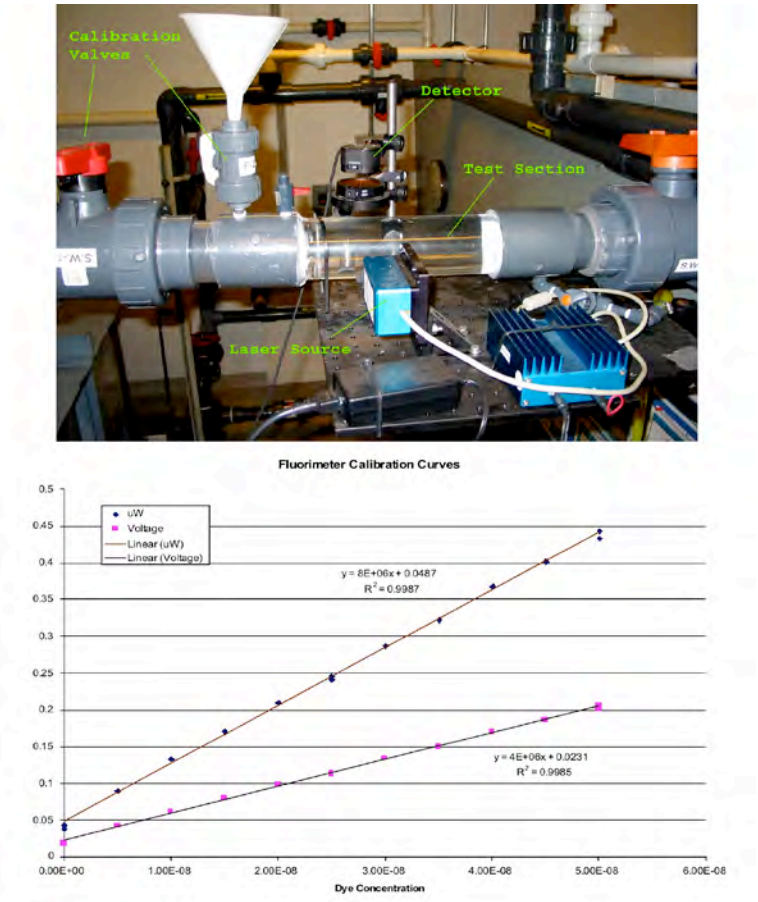

Figure 4. Fluorimeter setup and calibration curves. Ordinate is fluorimeter voltage (lower curve) or power (upper curve).

the conductivity sensors can only track the salinity changes during the latter portions of the experiment when water exiting the tank is at near-saltwater conductivity.

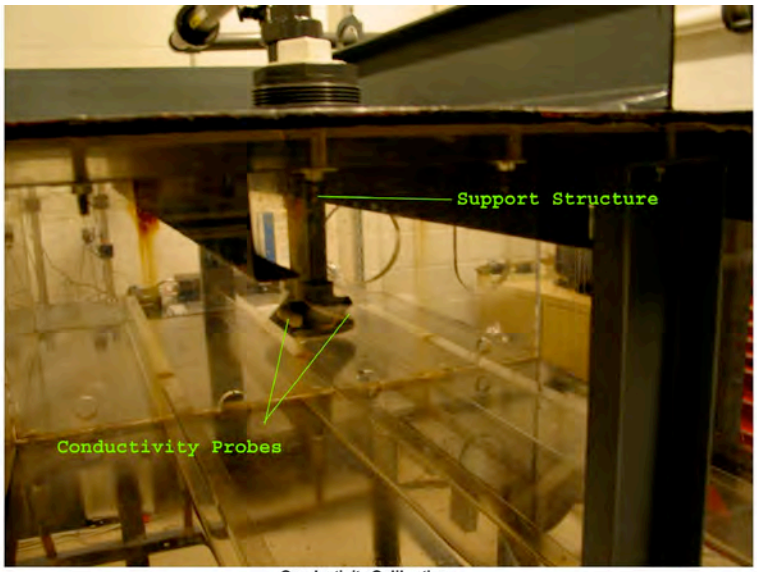

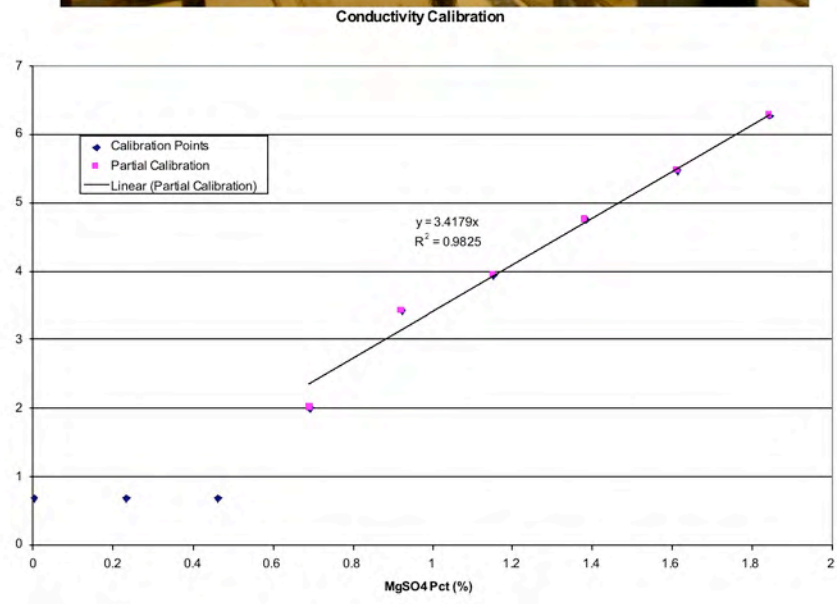

Figure 5. Conductivity sensor setup and calibration curves. Ordinate is voltage.

Data Processing

LIF data processing

The magnitude of data collected using LIF techniques requires a large amount of data processing to provide concentration history, estimates of mixing (mixedness), and volume of fluid calculations. The data processing calculations were performed on five dual-processor Pentium Xeon 3.0 GHz machines with 1.0 GB of RAM each. In order

to perform the necessary calculations, in-house-developed MatLAB[†] software was used to normalize the images and calculate the mixedness and volume of fluid levels. The separate data processing procedures are described in the following sections.

Image Renormalization

The raw LIF images were first normalized using information from the reference (full dye) and dark (no dye) images. The reference images and dark images were averaged over 100 frames to give statistically valid averages for each pixel. Each pixel in the raw data series was then renormalized from an 8-bit integer to a 16-bit integer ranging from 0 to 10,000 using the following equation,

$$N(x,y) = S\frac{I(x,y) - DF(x,y)}{BF(x,y) - DF(x,y)} \tag{1}$$

where $N(x,y)$ is the normalized value at each pixel, S is the scaling factor $(10,000)$, I is the intensity at each pixel, DF is the dark field value at each pixel, and BF is the reference value (full dye) at each pixel. An example raw data image is shown in Figure 6.

Figure 6. Example LIF raw data image from Camera 3 for Condition 2.

[†]©The MathWorks, Inc.

Volume Fraction and Mixedness

Volume fraction (v), defined as the relative amount of saltwater at each pixel location (x, y), is given by the following equation,

$$v(x,y) = \frac{N(x,y)}{S} \tag{2}$$

where $v(x, y)$ ranges from 0 (pure freshwater) to 1 (pure saltwater). v is calculated for every pixel in the interrogation region, and averaged to obtain the spatially averaged v in each measurement region.

While v gives the relative amounts of each of the fluids at each pixel location or averaged over each of the data planes, it provides no information about whether the two fluids are stratified or mixed. Mixedness, $M(x, y)$, quantifies the amount of mixing at each pixel or averaged over each data plane and is defined by,

$$0 \leq v(x,y) < 0.5 \quad : \quad M(x,y) = 2v \tag{3}$$

$$0.5 \leq v(x,y) \leq 1.0 \quad : \quad M(x,y) = 2(1-v). \tag{4}$$

$$\tag{5}$$

The mixedness function is shown in Figure 7. In a region that is purely stratified, the regions of pure freshwater or saltwater will have VF values of 0 or 1, respectively, which gives $M = 0$ in both cases. On the other hand, $v = 0.5$ will result in $M = 1$. At each time step, M is averaged over the entire data plane, resulting in a single value of M for each time step. The time series of these spatially averaged mixedness values are compared with the CFD simulation data.

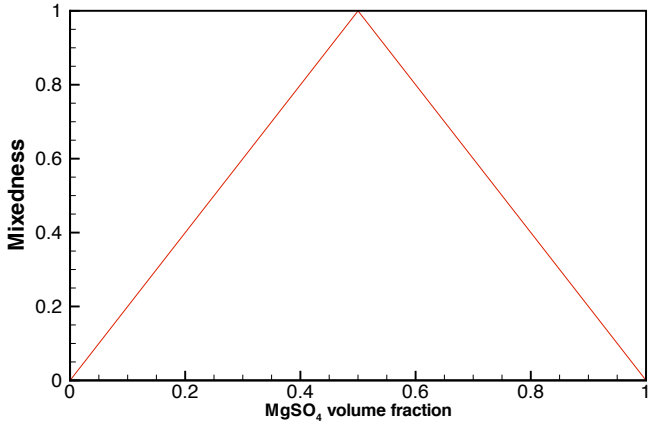

Figure 7. Mixedness as a function of $MgSO_4$ volume fraction.

Spatial and Temporal Filtering

The data shown in Figure 6 contains small-scale turbulent structures that make comparison to computational fluid dynamic (CFD) codes difficult. The raw LIF data

was spatially and temporally averaged to provide a smoothed experimental dataset for CFD comparisons. Spatial filtering was accomplished by applying a Gaussian filter ($\sigma = 32$, bin size 16). while temporal averaging was applied over a 2-second period centered at the measurement time.

Fluorimeter data processing

To process the fluorimeter data, dark data was collected prior to testing in order to provide a reference for background noise and a zero dye concentration measurement. The fluorimeter data collected at the beginning of the test were assumed to be pure alcohol solution. The data from the fluorimeter during the test were fit to a linear curve between the zero measurement and the pure alcohol solution measurement, assuming that the pure alcohol concentration had a value of 1 (or 100%) at the beginning of the test. This fit was performed in each test because the dye concentration was not identical throughout the test plan, and reference data were needed before each experiment. A sample fluorimeter voltage plot is shown in Figure 8.

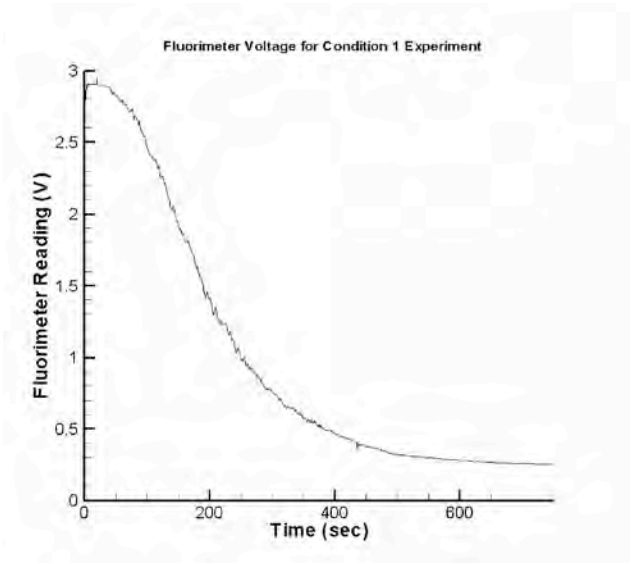

Figure 8. Example raw fluorimeter data for Condition 1.

Conductivity sensor data processing

To process the conductivity sensor data, the reading level when the tank was filled with pure $MgSO_4$ solution was used as a reference. A reading of zero was assumed for zero salinity, since an actual value of zero $MgSO_4$ was below the sensitivity threshold of the instrument. A linear dependence, confirmed by calibration, was assumed. All data below the sensitivity cutoff of the instrument were ignored.

EXPERIMENTAL RESULTS

Laser Induced Fluorescence

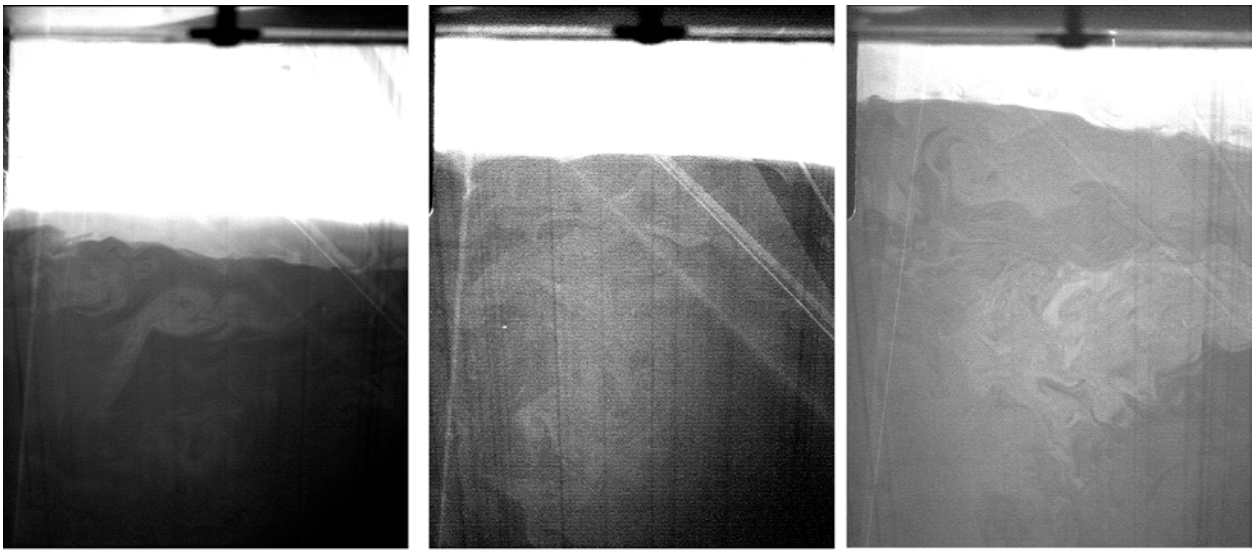

Figure 9. Mixing layers in the LIF raw data at $t^* = 0.5$. Mixing layers are the lighter gray regions.

General flow features

Several qualitative observations can be made from the raw LIF data, as turbulent structures, hideout, and the level of mixing within are readily visible. Mixing is one of the most important physical phenomena in ballast water exchange and the mixing layer between the two fluids is where the mixing takes place. Figure 9 shows renormalized images that have been enhanced to show the mixing layer for each test condition. The bright region at the top of each image represents the layer of freshwater remaining in the ballast tank whereas the shaded regions represent sections of the tank that are mixed with saltwater, with darker areas containing higher concentrations of saltwater. The tank top is also clearly visible. The mixing layer is much more dispersed in condition 2 than in condition 1, the latter being much thinner and localized. This stems from the larger density difference in condition 1, which inhibits mixing of the two fluids and creates a much more stable interface than in condition 2. This implies that decreasing the density difference between two fluids enhances the mixing process in the ballast water exchange process.

The effects of increasing flow rate can also be seen in Figure 9. When the flow rate is increased from 4.1 ℓ/sec (65 gpm) to 6.9 ℓ/sec (110 gpm) (condition 2 to condition

3), even more mixing is visible. This occurs because the incoming flow has much more turbulent energy with higher energy turbulent eddies that generate mixing, advecting mixed regions away from the interface. It should also be noted that as density difference decreases from condition 1 to condition 2, the layer of original fluid at the top of the ballast tank is much thinner. This is because the buoyancy forces between the two fluids are smaller requiring less energy to lift the regions of heavier fluid above the interface, where it remains in large part due to turbulent mixing processes.

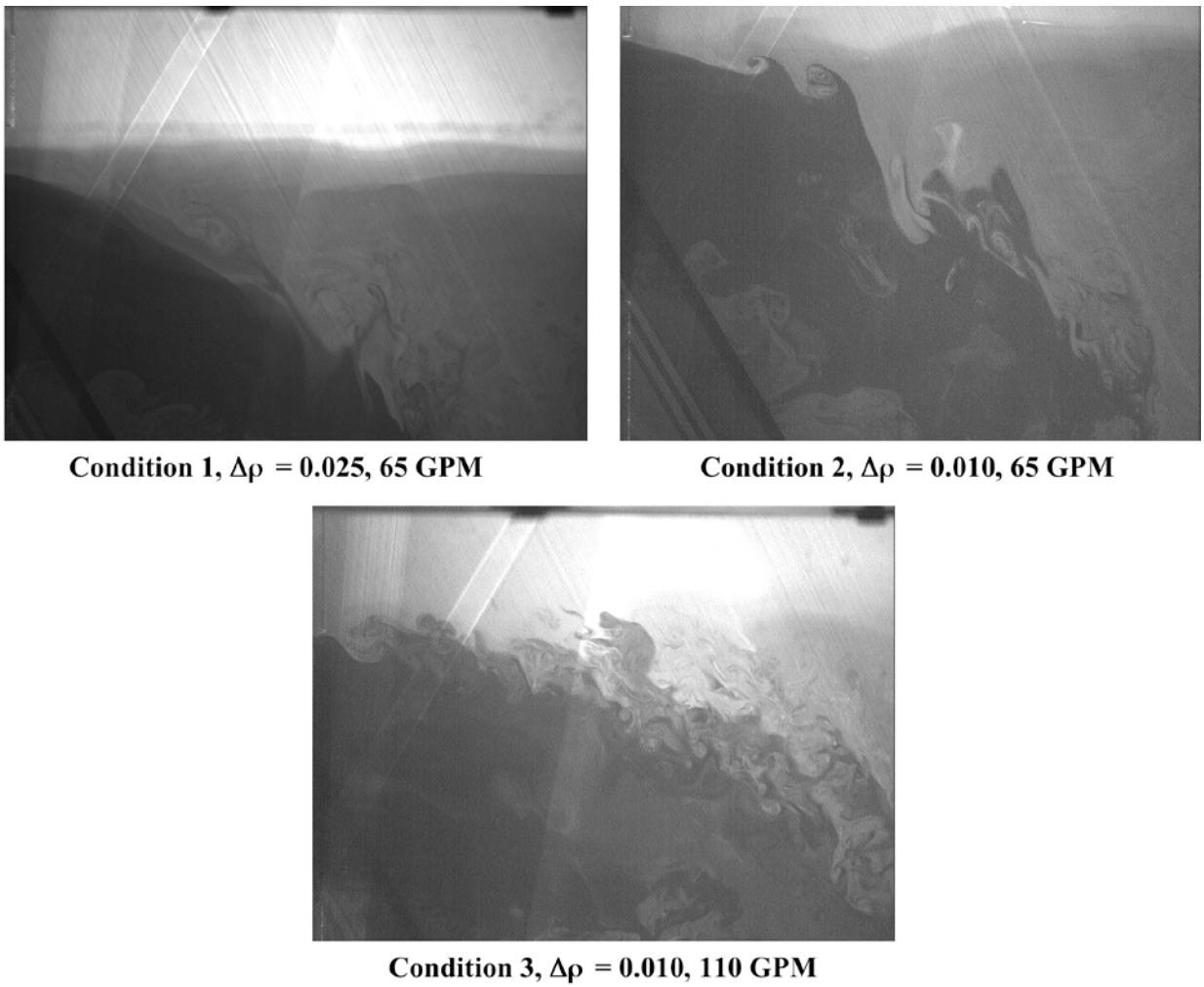

Figure 10. Jet exiting the manhole (left side of each figure) for each test condition at $t^* = 1$.

The flow structure of the jet exiting the manhole is shown in Figure 10 at $t^* = 1$. For condition 1, the large density difference causes the jet to spill through the manhole and fall quickly toward the bottom of the ballast tank. When the density difference is decreased (condition 2), the jet exits the manhole but has a larger horizontal component. When the flow rate is increased (condition 3), the jet exits the manhole and propagates

almost horizontally through the field of view. Another interesting observation is the composition of the fluid inside the jet. In condition 1, the jet is comprised mostly of incoming saltwater. In condition 2, the fluid inside the jet is more mixed, and in condition 3 the fluid inside the jet is almost completely mixed. The impingement of

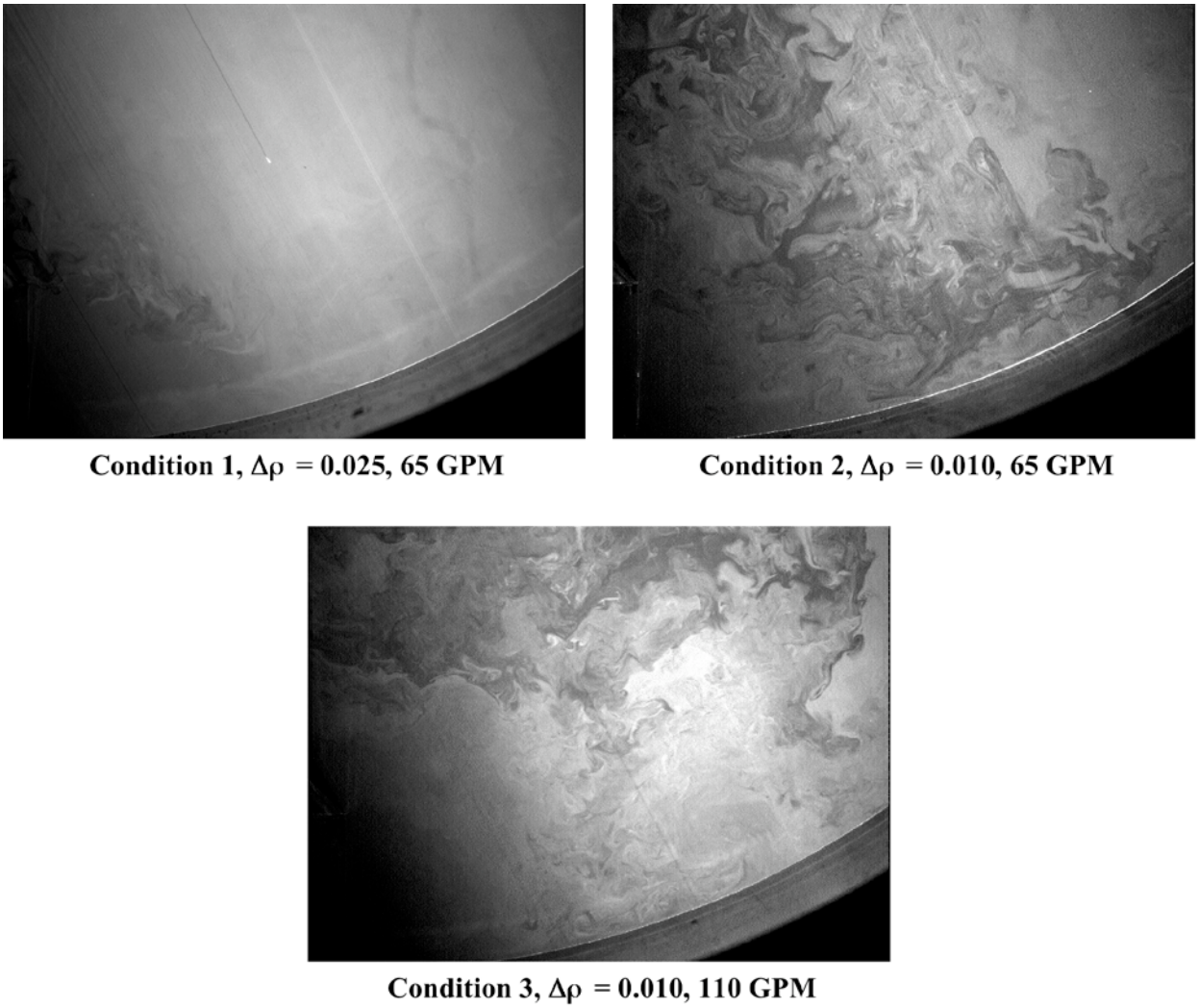

Figure 11. Jet impingement on side of HST1 for each condition. Flow enters from top left corner of each figure.

the manhole jet (Camera 4) on the rounded side of HST1 for each condition is shown in Figure 11. In condition 1, the jet impinges upstream of the stringer very close to the manhole, as expected with the large density difference. The jet in condition 2 impinges near the center of the field of view on the curved surface of the tank, and is also much more mixed than the jet in condition 1. For condition 3, the jet impinges further downstream and exhibits an even greater level of mixing.

Another important phenomenon encountered in BWE is hideout. Hideout is defined as the amount of pure original fluid trapped at the top of the tank at the end of an exchange. Figure 12 shows the LIF images for all three conditions at $t^* = 3$. It is evident that condition 1 exhibits the largest amount of hideout in this bay. For condition 2, the amount of hideout is decreased slightly. However, for condition 3, the hideout has been completely scoured from the bay due to a large increase in turbulent energy at the fluid interface due to the increased flow rate.

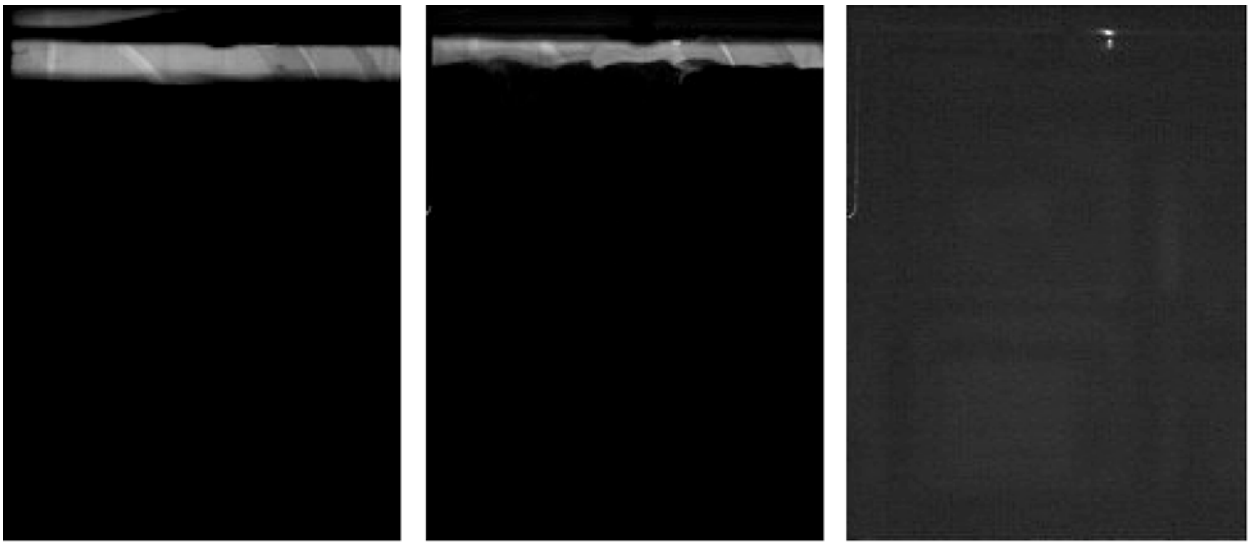

Figure 12. Hideout for (left) condition 1 (center) condition 2 and (right) condition 3.

Mixedness

Figure 13(a) shows the mixedness as a function of time for camera 1 for all conditions. Figure 13(a) shows that for condition 1, the mixedness level starts at zero, increases rapidly due to energetic mixing from the bellmouth jet and from the flow over the longitudinal stringer and persists for a much longer portion of the exchange than for conditions 2 and 3, not reaching a level of zero until $t^* = 2.8$. The mixing persists in condition 1 because a small mixing layer persists in camera 1 even as the dense fluid pushes the lighter fluid out of the field of view. When the density difference is decreased in condition 2, and the flow rate increased in condition 3, the initial mixing peak is much more pronounced reaching levels of almost 0.9. This is as expected because the decrease in density and increase in flow rate both increase two fluid mixing. For conditions 2 and 3 (Camera 1) the mixing decreases rapidly to zero at approximately $t^* = 1.1$ signifying that either the camera 1 region has become completely stratified or has become completely flushed of freshwater. As can be seen in the SWVF plot, Figure 14(a), the latter is the case, as the SWVF also goes to a value of 1 at $t^* = 1.2$. It should be noted that a mixedness value of one is not realized because the LIF measurement is an average of the entire field of view. Single pixels may reach a mixedness level of one,

but on average the entire measurement region never reaches the maximum mixedness value in the time frame of the experiments.

Figure 13(b) shows the mixedness as a function of time for camera 2 for all conditions. Camera 2 interrogates the upper portion of the bay upstream of the manhole as shown in Figure 1. Figure 13(b) shows trends that are very consistent with the trends seen in Figure 13(a). For condition 1, the mixedness values barely reach 0.3 indicating a highly stratified flow. Thus, condition 1 acts more like a plug flow, where the heavier liquid, saltwater, pushes the lighter fluid, freshwater, up and out of the tank, like a piston, with a minimum of mixing. In conditions 2 and 3, the mixedness reaches value of 0.6 and 0.8, respectively, due to mixed layers that are much thicker than for condition 1. For conditions 2 and 3 the mixedness falls more quickly than condition 1 to lower levels as the original fluid is diluted more quickly and the freshwater is more quickly removed from this region.

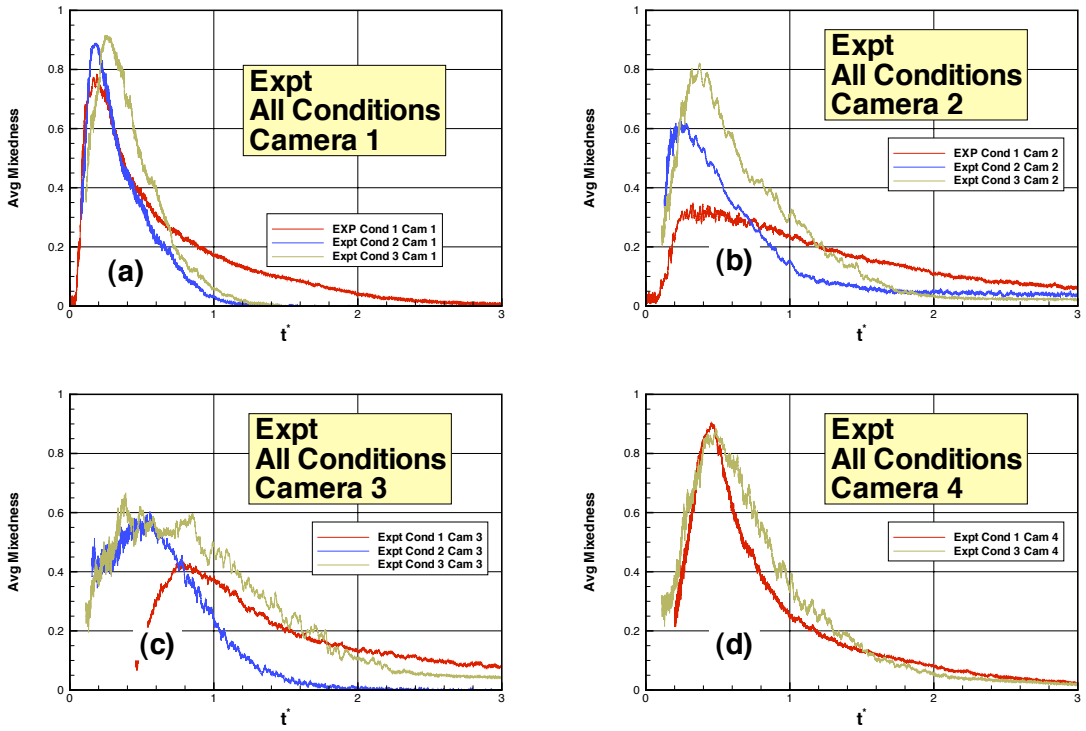

Figure 13. Experimental mixedness results for all conditions (a) Camera 1 (b) Camera 2 (c) Camera 3 and (d) Camera 4. The ordinate is mixedness and the abscissa is non-dimensional time, t^*.

Figure 13(c) shows the mixedness as a function of time for camera 3 for all experimental conditions. Camera 3 interrogates the flow exiting the manhole as shown in Figure 1. Figure 13(c) shows trends that are very consistent with the trends seen in Figure 13(a). In condition 1, as seen in Figure 10 the jet exiting the manhole has a

high SWVF, which falls vertically as soon as it exits the manhole. This results in a mixed region that persists throughout the exchange, as the jet impacts and fills the bay from the bottom of the tank. The jet mixing layer provides energy for mixing the fluid in the region between the original fluid and the incoming fluid, but it does not contain enough energy to mix the entire interrogation region. For condition 2, as seen in Figure 10, the jet exiting the manhole is much more mixed due to the enhanced mixing upstream. The jet propagates throughout much of the interrogation region, providing a large mixing region that spans most of this section of the tank. This allows the fluid to mix much more readily, and after a period of time the fluid is diluted and approaches $v = 0.95$ at $t^* = 1.6$. In condition 3, the mixing occurs at a faster rate, as turbulent mixing structures dominate the mixing phenomenon. The persistence of mixing seen in condition 3 is most likely due to local trappage, and mixing of original fluid at the bottom of the tank throughout the exchange.

Figure 13(d) shows the mixedness as a function of time for camera 4 for conditions 1 and 3. Camera 4 interrogates the region in which the jet from the manhole impinges on the curved portion of the bay. In this region for both conditions, the mixedness reaches values greater than 0.8 which are of the same magnitude as those reached in camera 1 shown in Figure 13(a) . This shows that the waterfall impingement on the curved side of the hopper side tank creates as much mixing as that generated near the bellmouth.

Saltwater Volume Fraction — Experimental Data

Figure 14(a) shows the SWVF in the lower portion of the bay upstream of the manhole. The slopes of the SWVF curves are very steep indicating that the saltwater is very effectively replacing the freshwater. Also, at this time (early in the exchange), essentially only the inlet bay is getting filled. In condition 2 (Figure 14(b)) the slopes of the SWVF curves for $t^* < 1$ are much less than for camera 1 indicating that freshwater is exiting much more slowly, which is due to the SW/FW interface reaching the bottom of the manhole and the saltwater beginning to flow into succeeding compartments, thus slowing the rate of interface rise. For $t^* > 1$ the slope of the curves approach asymptotic values determined by the amount of hideout at the tank tops. Condition 1 has the most hideout, whereas the conditions 2 and 3 have successively less. The higher flow rates and smaller density difference create more mixing that scours the freshwater out of the tank top.

The SWVF behavior at the top of HST1, downstream of the manhole, is shown in Figure 14(c). The SWVF reflects first the mixed fluids entering HST1 (conditions 2 and 3, $t^* < 0.4$). For $t^* > 0.4$, it shows the subsequent rise in the interface level at the manhole, with condition 1 and 2 having steeper slopes perhaps because the interface is sharper and condition 3 having the smallest slope because of the fuzzy interface between the SW and FW. Again we see for $t^* > 1$ the curves approaching asymptotic values, with condition 1 having a significant volume of hide out.

Figure 14(d), the SWVF at the bottom of HST1, shows that for conditions 1 and 3 the curves have relatively steep slopes due to fact that the increase in SWVF is due to the filling of the HST from the waterfall flow through the manhole. The rate should

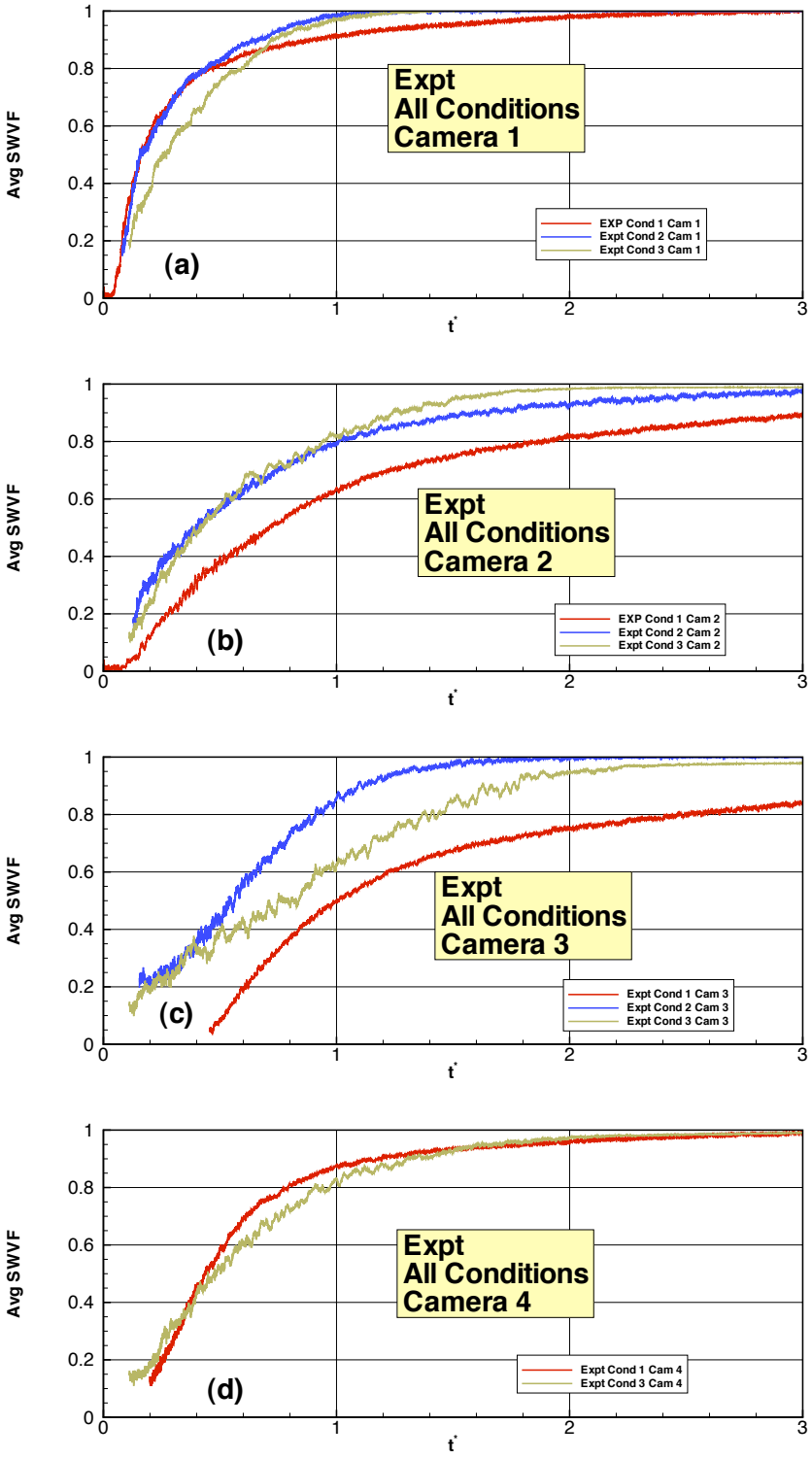

Figure 14. Experimental SWVF time histories for all conditions, from (a) Camera 1 (b) Camera 2 (c) Camera 3 and (d) Camera 4. The ordinate is SWVF and the abscissa is non-dimensional time, t^*.

be somewhat less than for camera 1, since when the inlet flow is diverted at this time into multiple bays, not just the inlet bay as for camera 1. The slope for condition 3 is less than for condition 1 because the two fluids are much more mixed.

Fluorimeter Results — Effluent Data

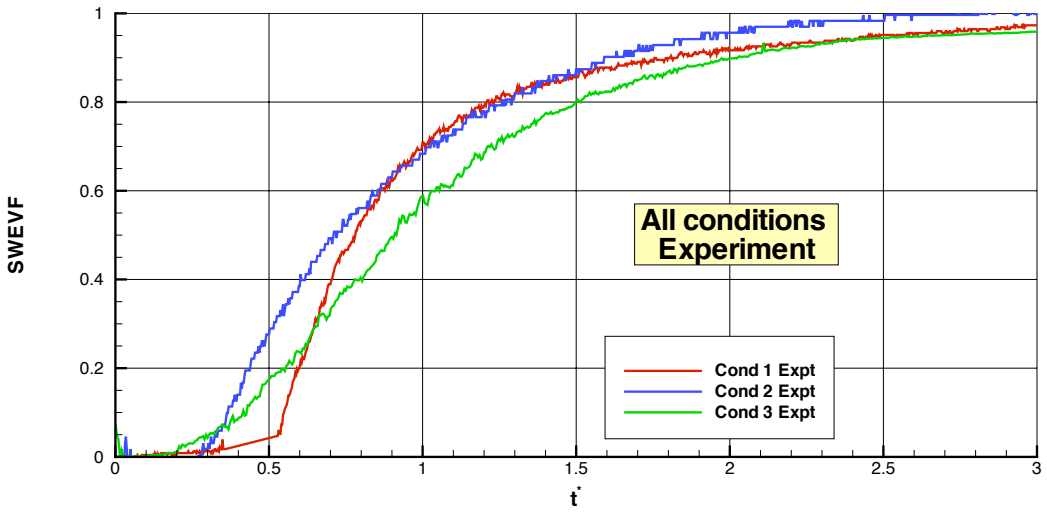

Figure 15. Experimental SWEVF (ordinate) as function of non-dimensional time, t^*, for all conditions.

Effluent concentration was measured in order to provide the saltwater volume fraction in fluid exiting the ballast tank as a function of time throughout the exchange. This is the type of measurement that could be taken during a full-scale shipboard experiment. The SWEVF is shown in Figure 15 for all of the experimental conditions. For all conditions there is a finite lag of about $t^* = 0.2$ before any SW reaches the exit. Condition 3 reaches the exit first because of the high levels of mixing in the inlet bay. SW reaches the exit last for condition 1 because it has the least amount of mixing in the inlet bay. However, for condition 1 once SW begins to arrive by $t^* = 0.5$, the increase in SWEVF is very steep as there is very little mixing and the curve reflects a rapid transition from almost all FW to almost all SW. Conditions 2 and 3 have successively smaller slopes due to increasing amounts of mixing which provides a longer transition time between the two almost-pure fluids. All curves eventually flatten out due to the scouring of FW that is trapped at the tank tops.

Conductivity Sensors

The conductivity sensors used in this experiment were intended as a proof of concept for possible use during full-scale experiments in the future. As mentioned previously,

only the latter portions of the experiment, where the$MgSO_4$ concentrations were relatively high, produced salinity readings greater than zero. The sensors tracked the salinity time history in compartment DB2. The normalized concentration of $MgSO_4$ solution as a function of time obtained by one of the conductivity sensors for conditions 1 and 3 is shown in Figure 16. It shows that for condition 1 there is an almost instantaneous increase in salinity at $t^* = 0.35$. CFD animations show that this is due to arrival of a very sharp two-fluid interface. Prior to this the salinity levels in the mixture above the interface are too low to register. After the interface goes above the sensor there is a slow increase in salinity as the two-fluid mixture beneath the interface becomes increasingly saline. The curve for condition 3 shows a later arrival (in terms of t^*) of the interface at about $t^* = 0.7$ while the average slope of the curve up to $t^* = 1$ is slightly less than for condition 1 indicating that there is more two fluid mixing beneath the interface than for condition 1. The CFD animations show that the interface is much more diffuse for condition 3 than for condition 1. It can be concluded that the behavior of the sensors matches up very well with the two fluid condition within the tanks, and such subtleties as the amount of mixing can be deduced.

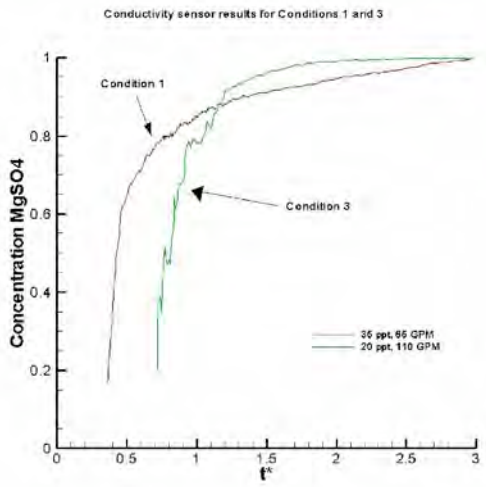

Figure 16. Conductivity sensor measurements of $MgSO_4$ concentration.

Discussion Regarding Experiments

Several important conclusions can be drawn from these experiments. The LIF data show that a decrease in density difference between the original ballast water and the exchanging saltwater allows increased mixing throughout the ballast tank. Increases in inlet flow rate also increase the amount of mixing throughout the tank. Increases in density difference can lead to increasing hideout of original fluid if the incoming flow does not have sufficient momentum to scour the pockets of trapped fluid from the tank tops. The effluent time histories suggest that exchanging fluids with large differences in density approaches the behavior of plug flow, whereas fluids of closer density approach a pure mixing condition as density difference is decreased and flow rate is increased.

The salinity probes appear to accurately track the qualitative two fluid condition within the tank.

COMPUTATIONAL METHODOLOGY

The CFD simulations were performed using the commercial viscous flow solver, Fluent.[‡] The code uses a cell-centered finite volume approach to solving the governing equations of mass and momentum. In addition, a transport equation is solved for the volume fraction of one of the fluids, with the algebraic constraint that the volume fraction of both fluids must sum to unity. The convection terms were discretized using a second order upwind method, while the diffusion terms were discretized using the second order accurate central differencing scheme. The turbulence closure used the RNG $k-\epsilon$ model. In order to solve for the physical and temporal distribution of the two fluids, the mixture multi-phase model is used. This is appropriate for this type of problem, where the two fluids are miscible, and have densities that are nearly equal. The time derivative terms were discretized using the first order backward implicit scheme. Currently this is the only method available for temporal discretization of the volume fraction equation. The PISO (Pressure-Implicit with Splitting of Operators) pressure-velocity coupling method was used, and the discretized equations were solved using Pointwise Gauss-Seidel iterations, with an algebraic multi-grid method to accelerate the solution convergence. A series of calibration runs were performed in order to arrive at the optimal set of run parameters. These were determined based on a comparison of the accuracy of the predicted mass flow of the incoming fluid relative to the theoretical value (equal to the inlet volumetric flow rate multiplied by the total elapsed time). In order to facilitate flexibility in handling the complex geometries in ballast tanks, an unstructured grid was developed to represent the physical tank model. A cut plane through the experimental model framework at the inlet pipe centerline showing the two-dimensional grid structure is shown in Figure 17. Only the inlet pipe, bellmouth, and exit pipe are modeled using structured hexahedral cells. This is for improved accuracy in predicting the inflow and outflow of the two fluids since the flow direction is mostly aligned vertically. The remainder of the domain volume is discretized using unstructured tetrahedral cells. The grid is also focused in regions of interest, such as near the inlet pipe and bellmouth and through the tank floor openings (e.g., manholes, limber holes) for improved resolution. The complete three-dimensional domain is composed of approximately 1.3 million cells in total.

ONE-THIRD SCALE CFD RESULTS

Figure 18 shows the predicted SWVF in the 1/3-scale tank for condition 1 across two cut planes (in color) through the experimental model ballast tank framework (gray). It shows that after 30 seconds (t^*=0.086) the SW is just beginning to fill the bottom of the inflow bay. At t^*=1.0 pure FW has been relegated to the tank tops, though there are large regions of mixed fluid. At t^*=2.0 the mixed regions have been flushed out of the tank and FW has been trapped in the tops of most of the bays. Finally, at t^*=3.0, much of the trapped FW (red) has been scoured away.

[‡]Fluent is developed by Ansys, Inc.

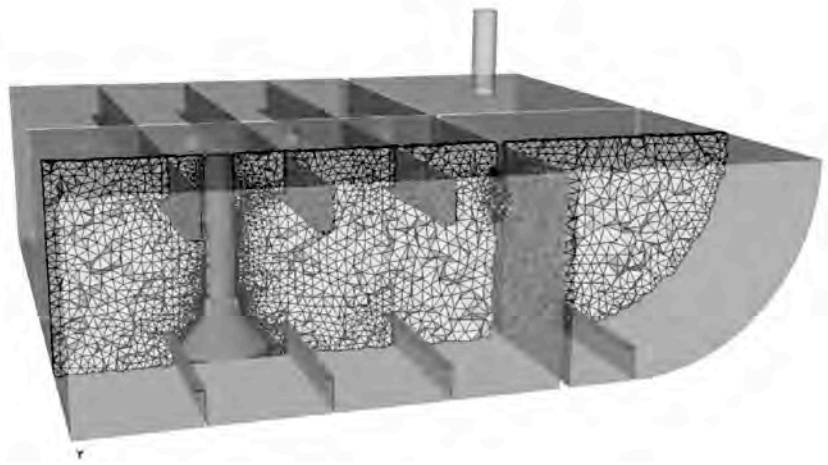

Figure 17. Grid details for 1/3-scale model.

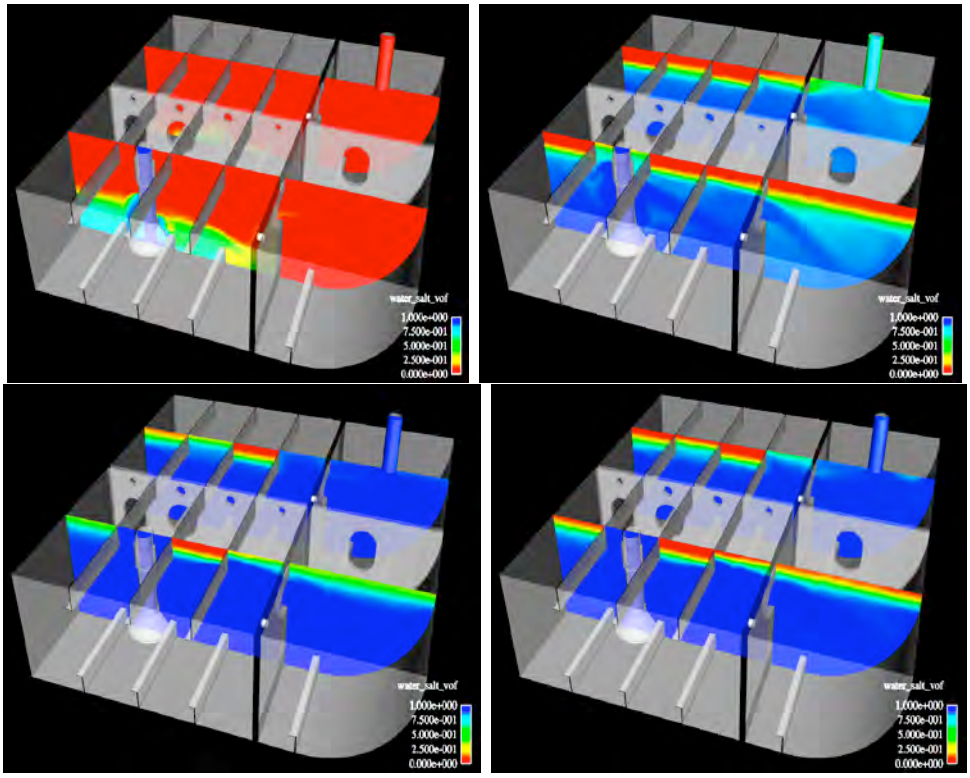

Figure 18. Three-dimensional views of 1/3-scale tank showing contours of SWVF from CFD simulations of condition 1; from upper left, proceeding clockwise: t^*=0.086, 1, 2 and 3. Blue represents SW, red is FW.

Figure 19 shows SWVF contours for condition 2 in which the density difference is lower than in condition 2. At t^*=0.086 it can be seen that the mixing region surrounding the bellmouth is less stratified than for condition 1. At t^*=1.0 the FW layers trapped in the tank are somewhat reduced from condition 1, particularly above the bellmouth, and upstream of the double-bottom/hopper side tank floor. Times t^*=2 and 3 show that the tank top has been scoured more completely than for condition 1.

For condition 3, Figure 20, at t^*=0.086, the influent SW flows completely to the tank top in the vicinity of the bellmouth. This leads to vigorous mixing and, as shown at t^*=1.0, the SWVF is much higher in the vicinity of the tank exit. At times t^*=2 and 3 the FW trappage is much less than for conditions 1 and 2, with only a single bay containing visible FW at t^*=3.

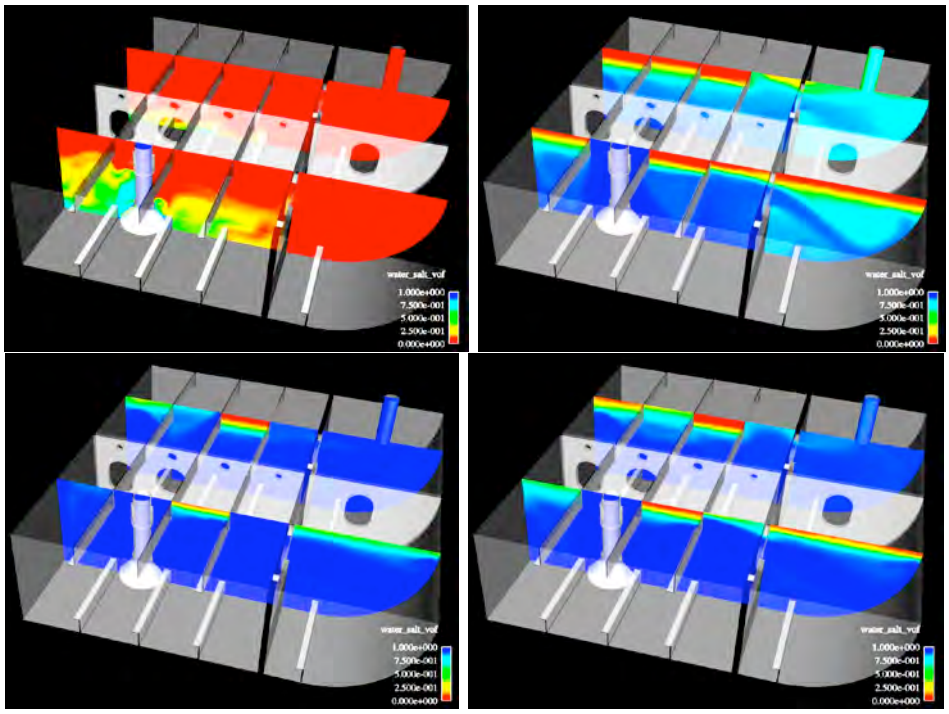

Figure 19. Three-dimensional views of 1/3-scale tank showing contours of SWVF from CFD simulations of condition 2; from upper left, proceeding clockwise: t^*=0.086, 1, 2 and 3. Blue represents SW, red is FW.

Exchange Efficiency (EE)

Figure 21 shows comparisons of EE from the CFD and experimental data for the three test conditions. EE is defined as the volume of SW in the tank divided by the tank volume. The CFD values of EE are computed directly by a spatial integration of the SWVF over all grid cells within the CFD tank model. On the other hand, the

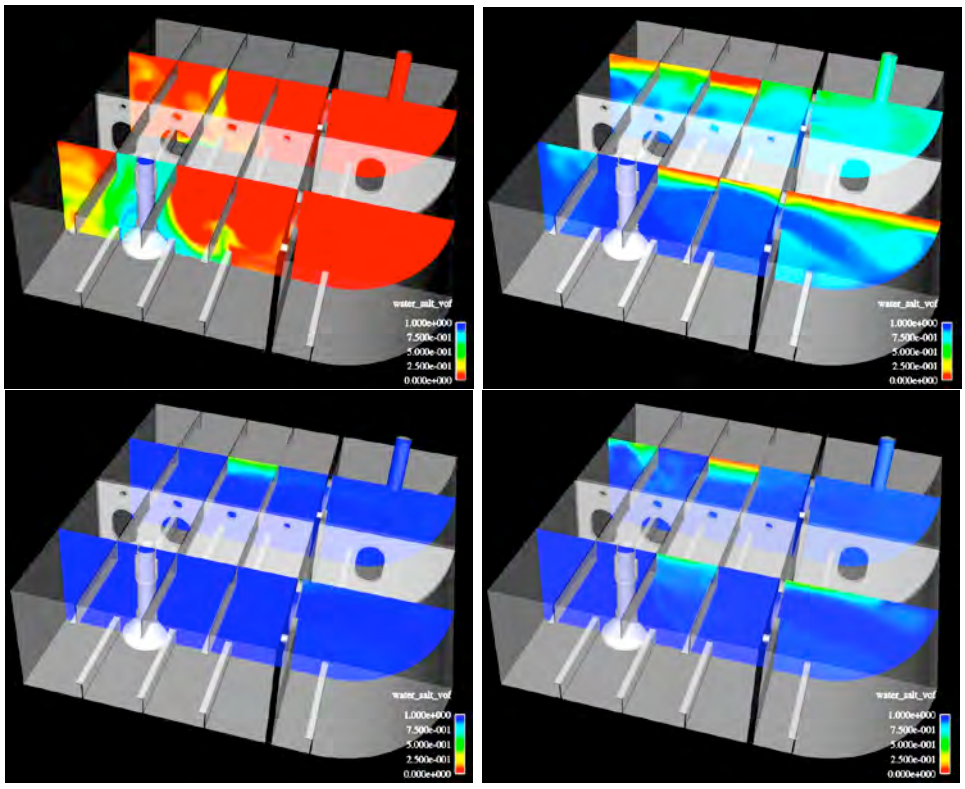

Figure 20. Three-dimensional views of 1/3-scale tank showing contours of SWVF from CFD simulations of condition 3; from upper left, proceeding clockwise: t^*=0.086, 1, 2 and 3. Blue represents SW, red is FW.

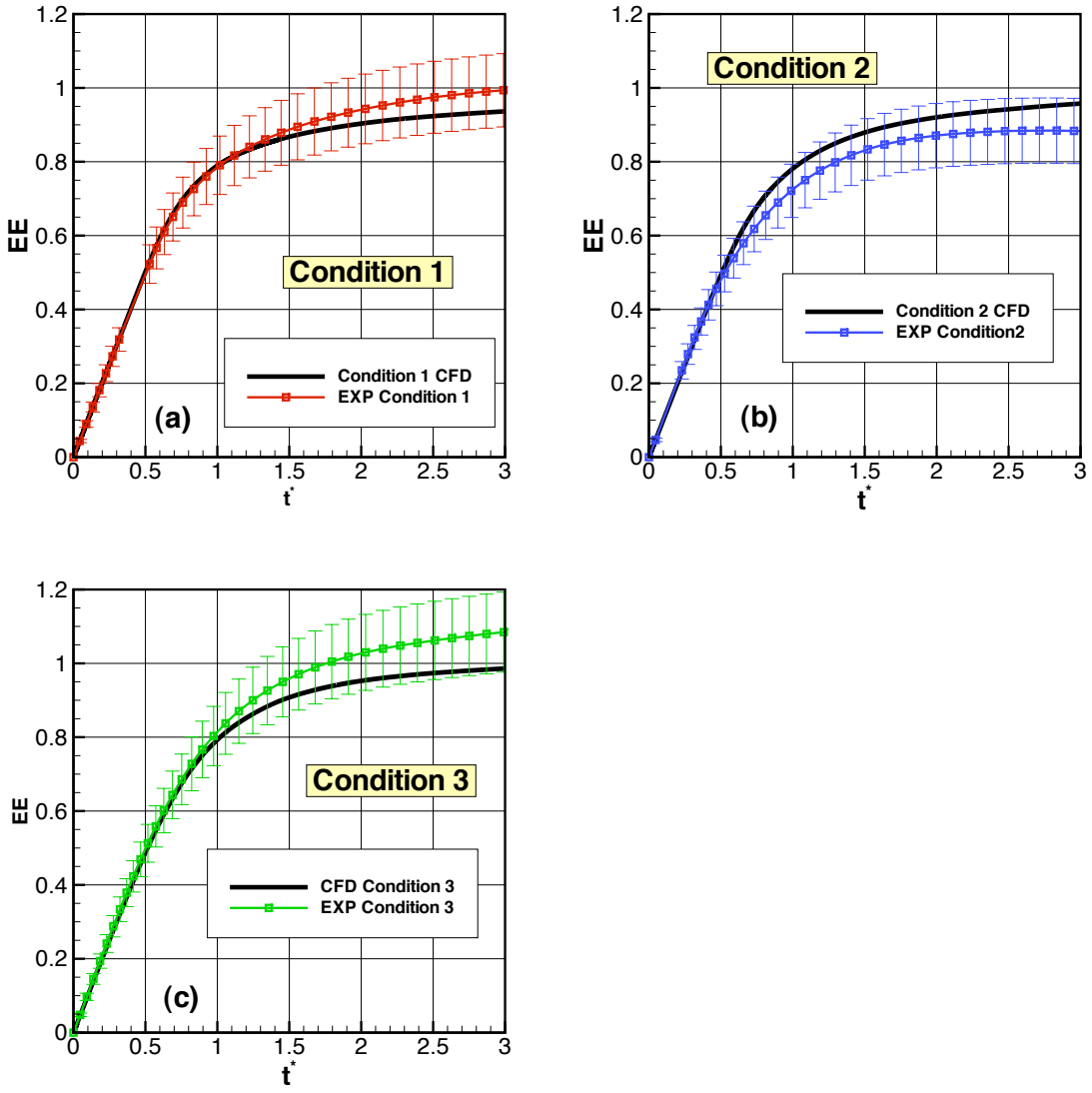

Figure 21. Predicted and measured EE (ordinate) for test conditions 1, 2, and 3.

experimental EE values are computed indirectly as the difference between the volume of SW entering the tank and the volume that has exited the tank:

$$EE(t) = \frac{V(t)}{V_o} = \frac{1}{V_o}\left[V(t=0) + Qt - \int_0^t Q\phi(\tau)d\tau\right] \tag{6}$$

where Q is the volume flow rate, V is the volume of SW in the tank, V_o is the volume of the tank, ϕ is the SWVF at the tank exit and τ is the dummy integration variable. The first term can be assumed to be zero since the tank initial condition is pure FW; the second term, for constant Q, is linear in time and the third term is the mixing term. If no mixing were to take place in the tank, then only FW would exit the tank, $\phi = 0$, and the mixing term would be zero. In this case $EE = 1$ would be achieved in a single TVE in what is called plug-flow filling. Since mixing does occur in the tank, $\phi \geq 0$ for much of the exchange and the term then represents the deviation of the exchange from plug-flow filling. The minimum value of uncertainty for the experimental values of EE are estimated to be 0.06, since that is the amount by which the Condition 3 experimental values of EE exceed the theoretical upper limit, 1.0. A formal uncertainty analysis should be performed in the future. Superimposed on the experimental curves are 10% uncertainty intervals. The CFD results are within these uncertainty intervals. The curves show that in the linear region (up to about t^*=0.50) CFD and experiment agree almost exactly. During this time the change in EE is proportional to the flow rate since there is no mixing and only freshwater is exiting the tank. For condition 1, the experiment and CFD agree until about t^*=1.2, after which the CFD predicts lower values, with a value of EE=0.93 at t^*=3.0. For condition 2, the experiment and CFD agree only to about t^*=0.60, after which the CFD predicts greater EE, with EE=0.96 at t^*=3.0. That CFD predicts higher values of EE for condition 2 than condition 1 makes physical sense because in condition 2 the mixing is much greater meaning that the volume of mixed fluid trapped in the tank tops will be less due to more energetic scouring. This is shown most clearly by comparing Figure 18 and Figure 19. For condition 3, the experiment and CFD agree to about t^*=0.80 after which the experimental EE values are much larger than the CFD EE values, with experimental EE increasing to a value greater than 1.0, which is physically impossible.

Figure 22 shows the EE results with the experimental curves and the CFD curves compared side-by-side. The CFD curves (right) show that the EE increases from condition 1 to 2 and again from 2 to 3. This must be due to the increased scour of the fluid trapped at the tank tops. The experimental curves, Figure 22(left) show a decrease from condition 1 to 2 and then a large increase from condition 2 to condition 3. This does not make physical sense. The differences between experimental and CFD model results and possible causes are discussed in the following sections.

SW Effluent Volume Fraction (SWEVF)

Figure 23 shows the SWEVF time histories comparing experimental and CFD values for each of the conditions. The uncertainty margin for the experimental data is shown. It appears that for condition 1, the CFD and experiment agree very closely up until $t^* =$

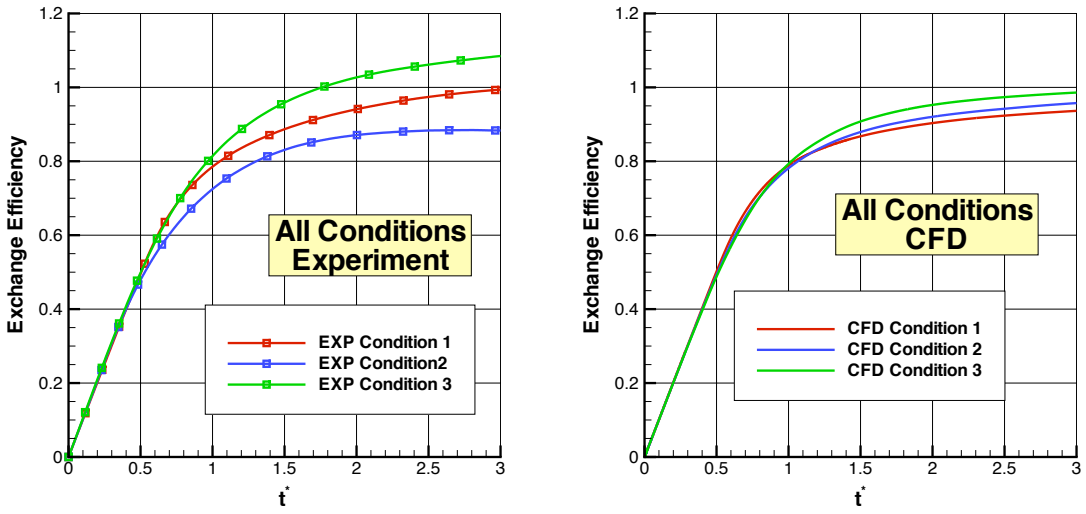

Figure 22. EE (ordinate) from experiments (left) and predicted by CFD (right) for all test conditions.

1.0, after which the CFD values become higher, though remain within the experimental uncertainty band. After $t^* = 1.0$ SWEVF is a reflection of the amount of scouring that is occuring between the FW trapped in the tank tops and the SW flowing to the exit. Less scouring will result in a SWEVF value closer to 1.0. More scouring would be indicated by values further from 1. Since scouring reduces the amount of FW in the tank, it will result in higher EE. In Figure 23(a) for $t^* > 1.0$ CFD predicts SWEVF closer to 1 than the experiments. Following the above reasoning, the cause of this must be that the CFD is predicting less scouring of the fluid trapped in the tank top, resulting in more freshwater trapped in the tank and less EE. Figure 21 shows that this is indeed the case i.e., after $t^* = 1$ the CFD EE curve is lower than the experimental curve indicating a greater volume of mixed fluid trapped in the tank top.

Figure 23(b), the SWEVF for condition 2, shows that early in the exchange ($t^* < 1.00$) the CFD is significantly lower than the experimental values. This indicates that the CFD is predicting less mixing during the early stages of the exchange than the experiment. During that middle stage of the exchange ($1.0 < t^* < 2.00$) the CFD and experiment agree almost exactly. Later in the exchange ($t^* > 2$) the experimental concentration is larger than the CFD predictions and goes slightly larger than the physical limit of 1.0.

Figure 23(c), the SWEVF time history for condition 3, shows that the experiment and CFD agree well for $t^* < 0.7$, after which the CFD predicts higher values than the experiment. This indicates that the CFD has less scouring of tank tops (and thus more mixed-fluid trappage) during the later parts of the exchange, and therefore, will predict less EE than the experiment. Figure 21(c) shows that this is the case, although the

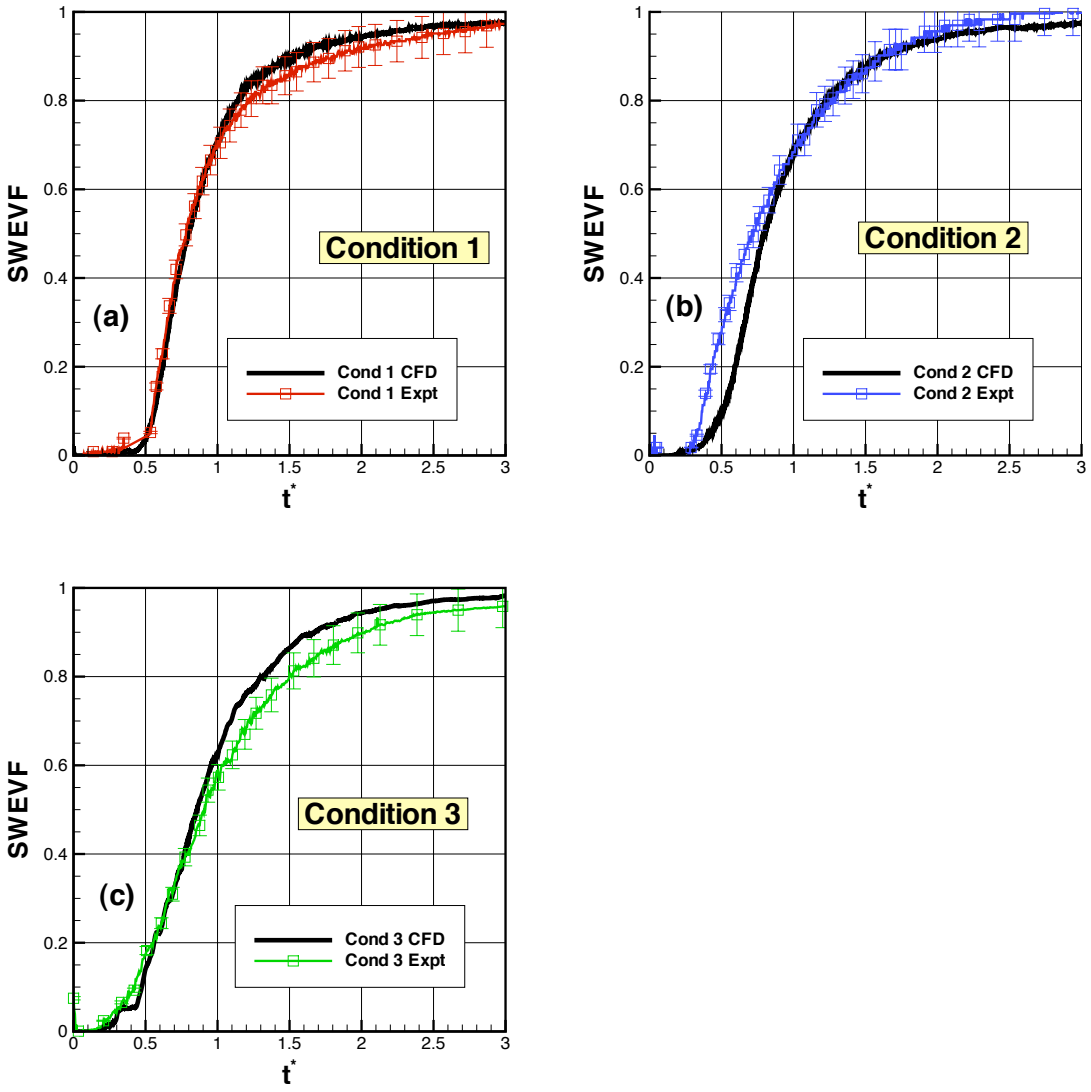

Figure 23. SWEVF (ordinate) time histories comparing experiment and CFD predicted values (a) condition 1 (b) condition 2 and (c) condition 3.

experimental values of EE for condition 3 are well above 1.0, which is the physical limit (maximum value) for EE. Table 5 summarizes the SWEVF values at integer multiples of t^*.

Table 5. SWEVF at selected times during exchange, comparing CFD and experimental values.

		t^*		
Condition		1	2	3
1	Expt	0.71	0.92	0.97
	CFD	0.71	0.94	0.98
2	Expt	0.68	0.96	1.01
	CFD	0.69	0.94	0.98
3	Expt	0.59	0.90	0.96
	CFD	0.63	0.94	0.98

Figure 24(b), the CFD predictions of SWEVF vs. t^* for the three conditions, shows that the three curves behave consistently with respect to the mixing that occurs in tank. For condition 1, which should have the least amount mixing due to the lower flow rate and higher density difference, the CFD predicts the latest arrival of SW at the tank exit ($t^* = 0.4$) of the three cases. For conditions 2 and 3 the first arrival of SW at the tank exit occurs at about $t^* = 0.25$, with condition 3, which has the highest flow rate and lowest density difference, having the highest SW concentration. The energetic mixing in the inlet bay results in mixed volumes that quickly advect to the tank exit. The order of the curves changes at $t^* = 0.65$ indicating that the cases with higher mixing early on have less mixing later on. At this point in the exchange, experimental movies show that the two fluids are highly stratified and the primary means of mixing is due to horizontal shear flows at stratified shear layers. Condition 1, with lower velocities and higher density differences will have less scouring at the two-fluid interfaces, meaning that the SW will pass through the tank with less freshwater contamination, and thus, show higher values of SWEVF at the exit. On the other hand, condition 3, with the highest velocities and lowest density differences, had the lowest values of SWEVF since it has increased mixing and FW contamination, leading to lower values of SW concentration at the exit. Condition 2 should be between conditions 1 and 3. At the later stages of the exchange ($t^* > 2$) the three conditions have identical SW concentrations, indicating that the CFD model, despite the differences in flow velocity and density difference, is predicting identical scouring between the SW and the FW hideout in the tank tops.

The experimental curves for the three conditions are shown in Figure 24(a). The curves for conditions 1 and 3 are consistent with respect to the two-fluid mixing that occurs in the tank as discussed in the previous paragraphs. Mixing in the inlet bay early in the exchange leads to early arrival of SW at the exit, with the highest mixing condition 3 arriving the earliest ($t^* \sim 0.2$); after $t^* > 0.65$ condition 1, with less mixing

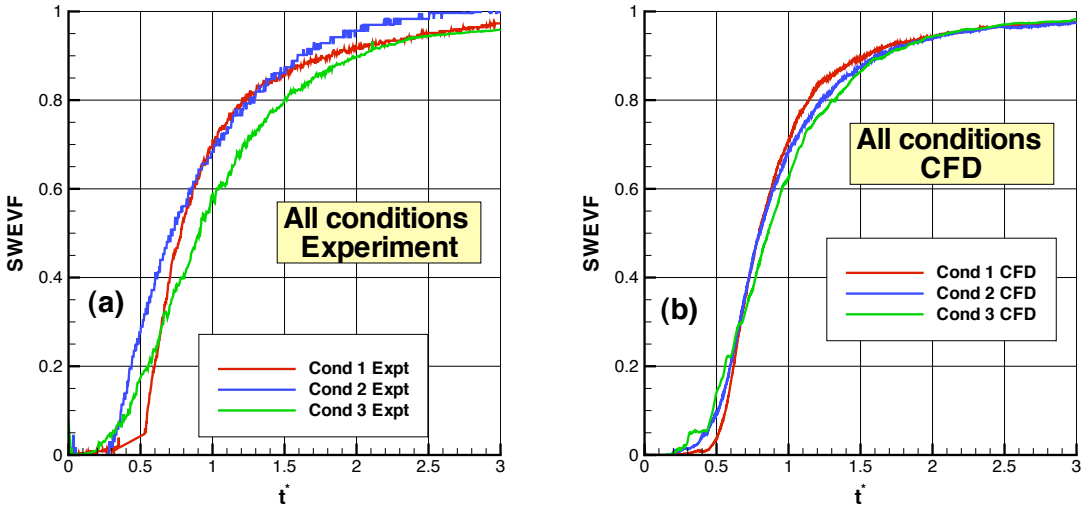

Figure 24. SWEVF (ordinate) time histories for all test conditions; (a) from experiment and (b) predicted by CFD.

at stratified interfaces, has higher values of SWEVF because the SW passes through the tank with reduced levels of FW contamination. The curve for condition 2 is inconsistent with these physics — after the first arrival of SW at the exit, the experimental condition 2 curve has SWEVF levels significantly higher than condition 3 for which the highest levels of mixing are expected. Even after the flows are completely stratified ($t^* > 1$) the condition 2 curve is higher than the condition 1 curve. Very late in the exchange ($t^* > 1.5$) condition 2 has higher levels than the other two conditions indicating that nearly pure SW is exiting the tank. This is inconsistent with the physics — if any condition is likely to have pure SW exiting the tank at that time, it would be condition 1. Furthermore, the experimental (measured) SWEVF for condition 2 actually went greater than 1.0, which is physically impossible. Thus, it is hypothesized that the experimental SWEVF for condition 2 has a positive bias error leading to a greater magnitude for the mixing term, ϕ, in the evaluation of the EE, which results in lower than expected EE values, as shown in Figure 22(left).

Full-scale shipboard experiments often use SWEVF to approximate EE. SWEVF is relatively simple to obtain since it is a point measurement whereas actual EE should be calculated by integrating the entire tank volume or by a time integration of the measured SWEVF. The following discussion addresses whether this is an accurate prediction methodology. A comparison of the EE and SWEVF as predicted with CFD is shown in Table 6. If perfect and instantaneous mixing occurred throughout the tank then the EE and SWEVF would be equal. The table shows that early in the exchange ($t^* = 1$) the EE values, calculated by CFD integrated over the entire tank, are significantly higher than the SWEVF. Even though energetic mixing is occurring in and around the

inlet bay, the mixed regions take a finite time to reach the tank exit and therefore, the SWEVF will be primarily FW during the early stages of the exchange, and it is not a good indicator for the integrated SWVF within the tank. Later in the exchange ($t^* = 2$), it can be seen that the EE and SWEVF compare very well, particularly for conditions 2 and 3 that have lower density differences and/or higher flow rates. Finally at end of the exchange ($t^* = 3$) the EE are less than the SWEVFs for conditions 1 and 2, due to the hideout, whereas they are practically the same for condition 3 due to lack of hideout. It can be concluded that the using SWEVF to approximate EE does not take into account the spatial inhomogeneities with in the tank, underpredicting the EE early on and over-predicting EE later on. For the case where the density differences are small, however, SWEVF can start to approach EE, in the mid- to later stages of an exchange.

Table 6. Comparison of EE and SWEVF predicted with CFD.

		t^*		
Condition		1	2	3
1	EE	0.79	0.90	0.94
	SWEVF	0.71	0.94	0.98
2	EE	0.78	0.92	0.96
	SWEVF	0.69	0.94	0.98
3	EE	0.79	0.95	0.99
	SWEVF	0.63	0.94	0.98

Saltwater Volume Fraction — Predicted vs. Experiments

The saltwater volume fraction (SWVF) averaged over the camera data planes from each experiment (Conditions 1-3) and that predicted by CFD are shown in Figures 25-27. SWVF is a measure of the relative amount of exchanged SW in a given area averaged over the data plane of the camera. The saltwater may arrive at the data plane either through a stratified flow along the tank bottom or in the form of a mixture.

Condition 1. Figure 25 shows the SWVF for Condition 1. Videos from the experiments show that the SW flows over a stringer into the Camera 1 data plane first as a highly diffuse mixture consisting of complex turbulent eddies beginning at $t^* = 0.04$ and then begins pouring over the stringer at about $t^* = 0.10$, increasing to full strength $t^* = 0.3$. Finally, at $t^* = 0.3$ Camera 1 becomes full of mixed fluid and the interface disappears. In Figure 25(a), the experiment and CFD both record the arrival of SW $t^* = 0.04$ with a mild slope, indicating a diffuse mixture. At $t^* = 0.10$ the slope in the CFD predictions increases indicating the arrival of the interface into the data plane. The experimental slope remains fairly constant. This difference in slope indicates that the CFD is predicting a less diffuse solution filling the bottom of the data plane, whereas the experimental data indicates a more diffuse mixture. We can deduce that the computations have under-predicted the amount of mixing that occurs upstream of the data

plane, presumably at the inlet. The predictions have much smoother spatial VF distributions because the turbulent eddies have been modeled. It appears, however, that the higher values of VF for the predictions are because the SW flow over the stringer is a stronger coherent jet in the predictions while the experiment shows a weaker more diffuse jet flow. This discrepancy persists until well into the filling, $t^* = 2$, when both the experiment and predictions converge to 1.0, i.e., when the entire data plane consists of SW.

Camera 2, Figure 25(b), tracks the SWVF in the top of DB1 upstream of the manhole between DB1 and HST1. From the experimental videos it can be seen that the first significant SW intrusions begin at the bottom of Camera 2 at about $t^* = 0.1$; at about $t^* = 0.2$ the flow becomes stratified with a thick and wavy mixed layer between the SW and FW regions; at about $t^* = 0.7$ the mixed layer has disappeared and the SW and FW regions are separated by a sharp, quiescent interface. These same features are also seen in CFD animations. The predictions have the same slope as the experiments though they have a small constant offset. The offset indicates that the CFD may be predicting a thinner mixed layer at first (thus, greater amount of SW in the Camera plane) than is measured in the experiments.

The Camera 3 data plane is directly downstream of the MH between DB1 and HST1. Experimental videos show that the first trace amounts for SW start flowing through the MH at $t^* = 0.1$ and the bulk interface begins pouring through the MH at about $t^* = 0.4$. The jet through the manhole is turned downward by gravity having a smooth interface until it turns about 45^0, where transition from a laminar to turbulent interface takes place. The videos show that HST1 fills from the bottom with a very diffuse mixed mixture never displaying a sharp interface. The jet through the MH is surrounded by a mixture of constantly increasing SW which decreases the gravity force on the jet, so that the downward component of the jet eventually disappears at about $t^* = 1.5$. CFD animations show that the gross flow features of the computations compare very well with experiments. In Figure 25(c), the CFD has a very small slope from $t^* = 0.08$ until about $t^* = 0.4$ which is due to the inflow of a very diffuse mixture. After this, the slope increases rapidly, so that it has a constant slope past $t^* = 1$. However, overall the CFD predicts significantly higher VF than is measured in the experiments. As the VF in the HST1 is a complex result of mixing in DB1, mixing at the interface of the MH jet and impingement of the jet on the bottom of HST1, it is difficult to pinpoint any one cause for the discrepancy. In view of the fact that the trends in the experimental SWVF are different than for the other three conditions, it may be the case that there is a systematic error in the experimental Camera 3, Condition 1 results.

Condition 2. Condition 2 has a smaller density difference between the two fluids but the same flow rate as Condition 1. Therefore, we expect the SWVF time histories to reflect greater mixing.

Figure 26(a) shows the SWVF time histories for Camera 1. We see that for Cameras 1 and 2 the experiment and CFD compare very well. This suggests that the CFD is better at simulating the greater mixing allowed by the smaller density difference. For Camera 3, the curves are parallel but offset, with the experimental SWVF greater than

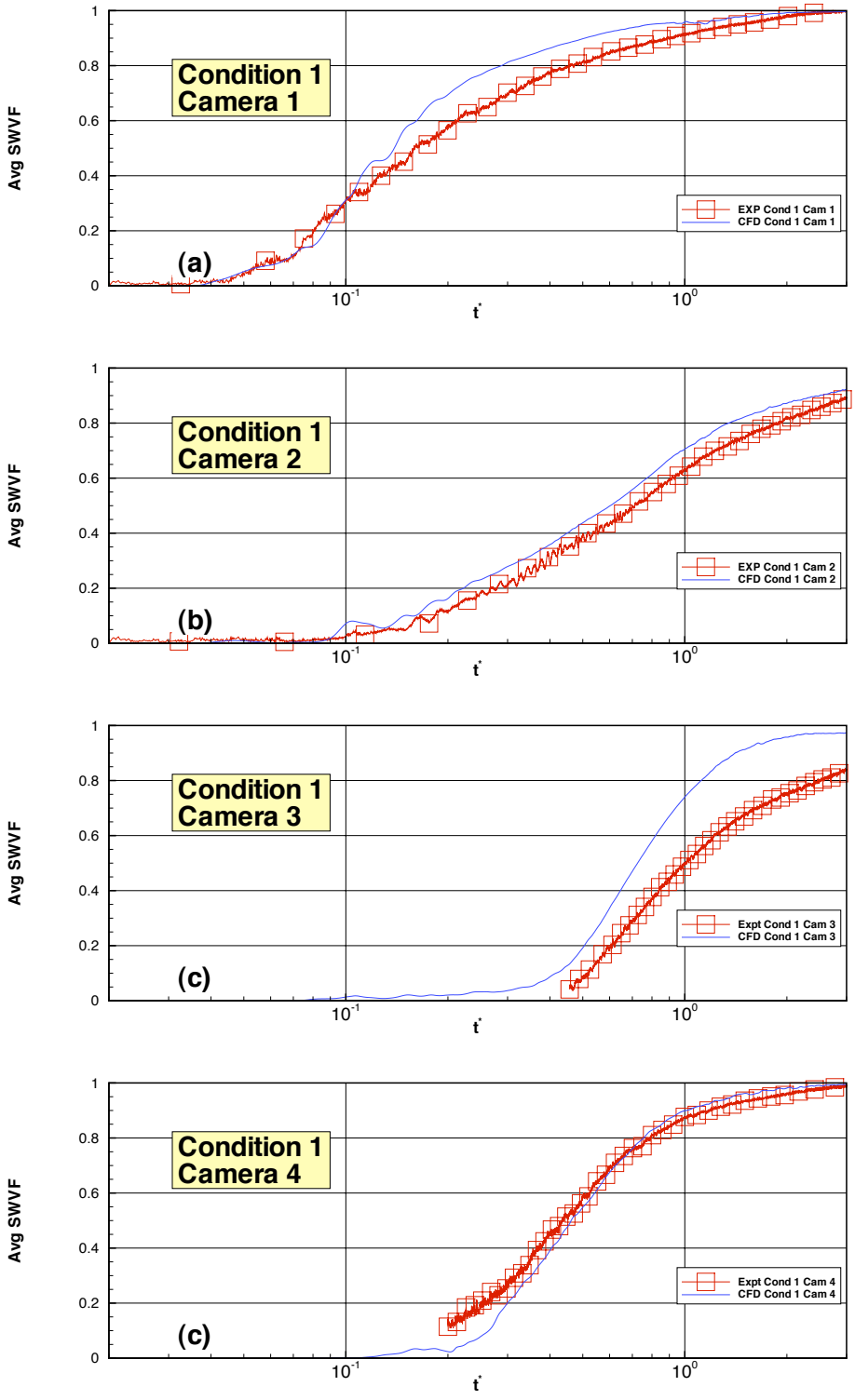

Figure 25. Area-averaged experimental and CFD SWVF time histories (logarithmically scaled) for condition 1; (a) Camera 1 (b) Camera 2 and (c) Camera 3.

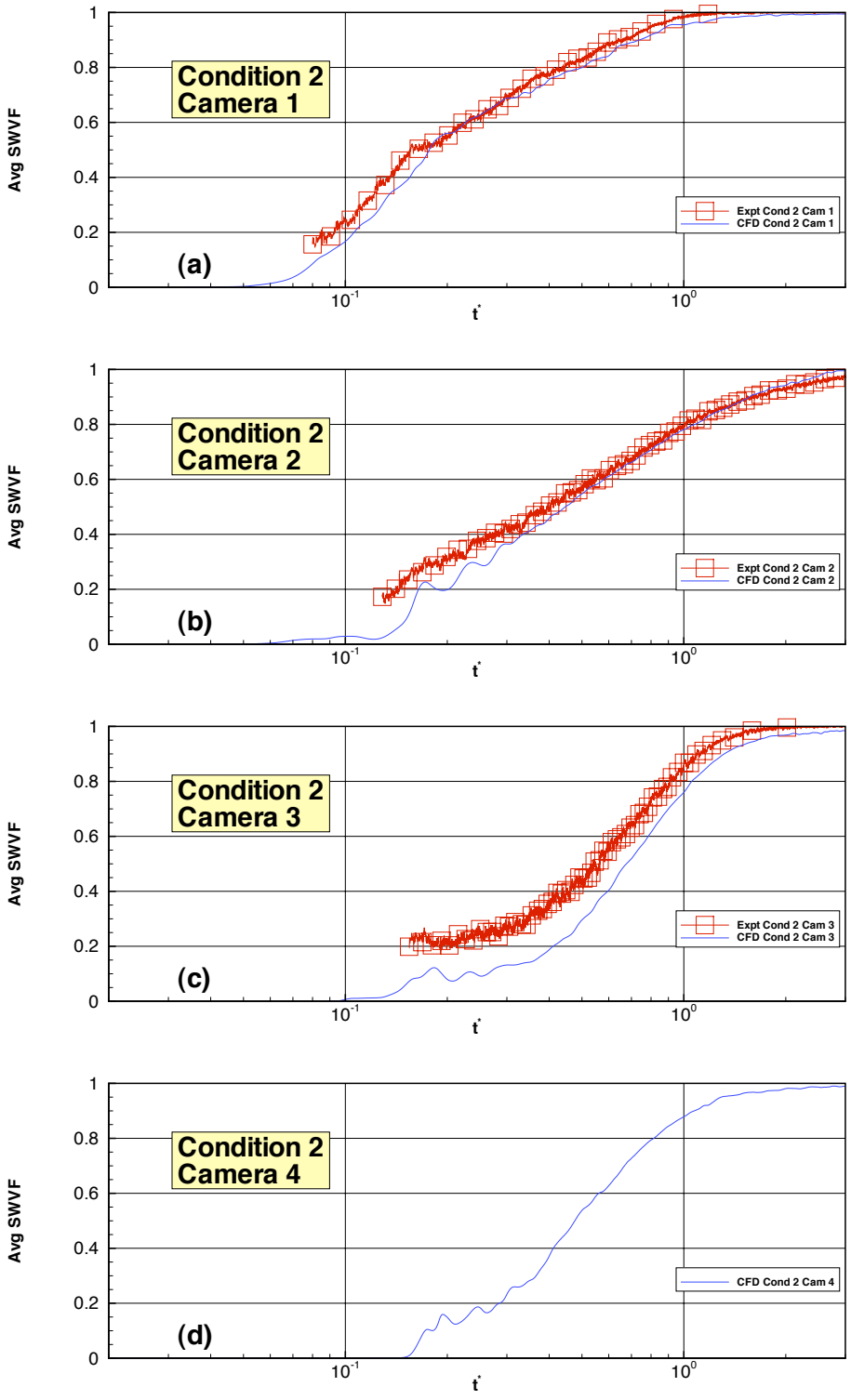

Figure 26. Area-averaged experimental and CFD SWVF time histories (logarithmically scaled) for condition 2; (a) Camera 1 (b) Camera 2 (c) Camera 3 and (d) Camera 4.

the CFD results. This suggests that HST1 fills faster in the experiment than in the CFD simulation. From the VF alone it is not possible to ascertain why. This will be discussed later in light of the mixedness results.

Condition 3. Figure 27 shows the SWVF time histories for Condition 3. The comparisons for Cameras 1 and 2 are very good over almost the entire filling. For Camera 3 the slope of the CFD is steeper than the experiment and the experimental data are approximately linear for $t^* < 1.6$. It is unclear as to the reasons for this behavior. Camera 4, on the other hand compares very well. The experimental data behavior is not consistent with Conditions 1 and 2.

Mixedness — Predicted vs. Experiments

Figure 28 is the mixedness for Condition 1 averaged over each of the four camera planes (see Figure 1). It shows that the experiment and CFD are, for the most part, in very good agreement, especially for the shape of the curves, and the magnitude and timing of the peaks. Camera 1, Figure 28(a), which is in the bottom of the inlet bay upstream of a manhole quickly receives highly mixed fluid due to mixing at the bellmouth. Camera 2, Figure 28(b), is above camera 1, upstream of and in direct alignment with a manhole. Arrival of mixed fluid is delayed, and the maximum mixedness is smaller because the flow has stratified after reaching the level of the manhole. Camera 3, Figure 28(c), is directly downstream of the manhole and almost the same height off the bottom as Camera 2. The CFD predicts slightly higher maximum mixedness than measured in the experiment. Camera 4, Figure 28(d) is where the manhole flow strikes the side of the tank, which causes high levels of mixing.

For condition 2, Figure 29, the CFD and experiment compare very well except at Camera 3, Figure 29(c), where the CFD mixedness peak has the same magnitudes but lags in time. There is no experimental data for Camera 4. Cameras 1 and 2 have significantly higher levels of mixing than Condition 1, due to the smaller density difference between the two fluids. Interestingly, for Cameras 3 and 4 in HST1 the mixedness for Condition 2 is only slightly higher than for Condition 1. It is reasoned that the more stratified water fall through the MH impacting the bottom of HST1 for Condition 1 acts as an energetic mixing mechanism, whereas for Condition 2, the water fall is much more benign since the flow through the MH is already mixed.

For condition 3, Figure 30, the experiment and CFD curves are in agreement in all four camera planes with respect to the general shape of the curves and approximate timing of the peaks. However, the CFD predicts smaller peak values and generally under-predicts mixedness. The reason could be that the CFD model does not adequately represent the complex, turbulent mixing associated with the higher flow rate and the smaller density difference.

A sense of the physical trends between the three conditions can be seen in Figure 31 which plots all the conditions in a single plot for each camera plane in linear-linear space. The experimental data are found in the left column; the CFD data in the right column. For Camera 1 it can be seen that a high level of mixing occurs very early during the exchange, with the magnitude of the peak increasing with increasing flow rate and/or

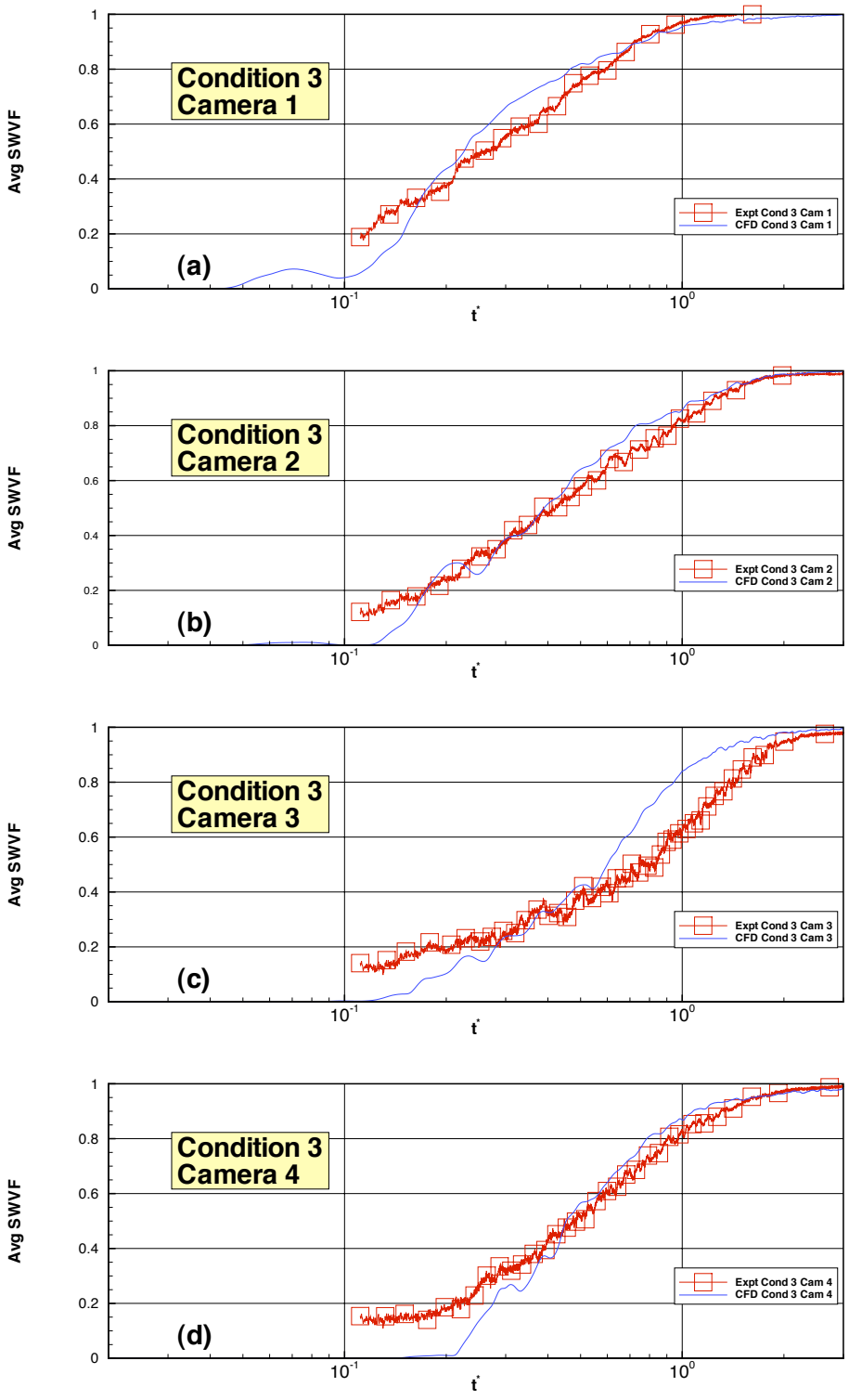

Figure 27. Area-averaged experimental and CFD SWVF (ordinate) time histories for condition 3; (a) Camera 1 (b) Camera 2 (c) Camera 3 and (d) Camera 4.

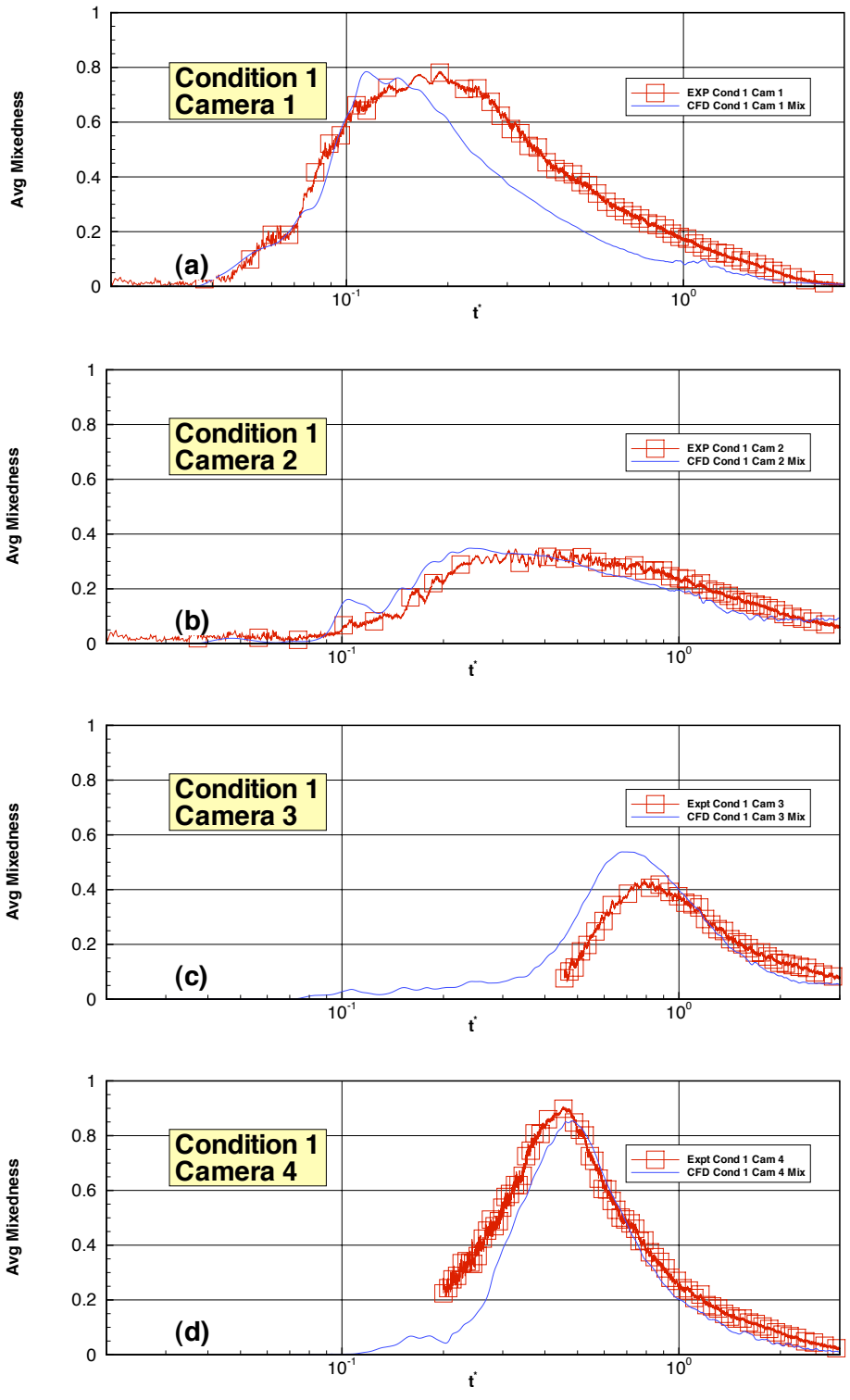

Figure 28. Area-averaged experimental and CFD mixedness time histories for Condition 1; (a) Camera 1 (b) Camera 2 (c) Camera 3 and (d) Camera 4.

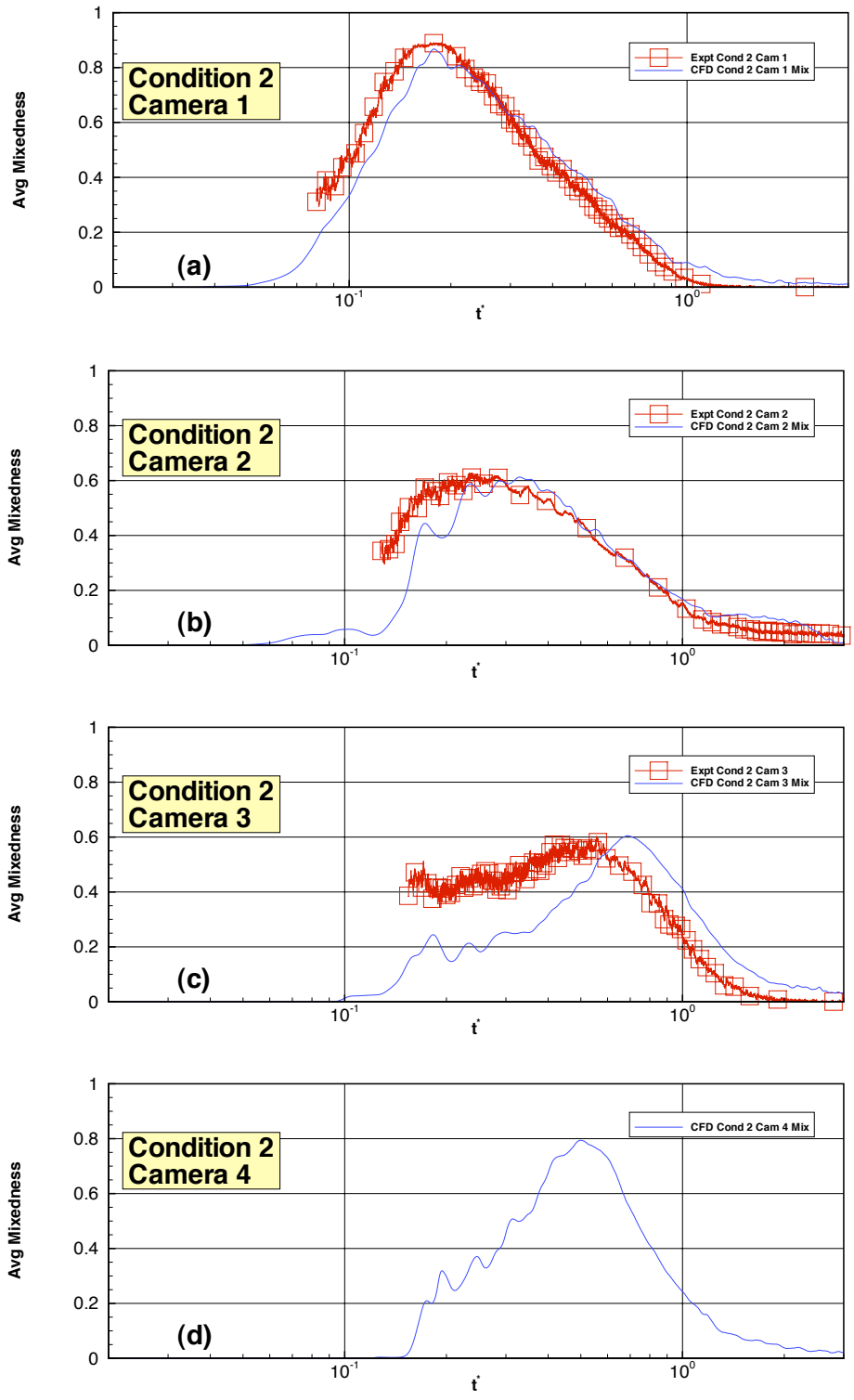

Figure 29. Area-averaged experimental and CFD mixedness time histories for Condition 2; (a) Camera 1 (b) Camera 2 (c) Camera 3 and (d) Camera 4.

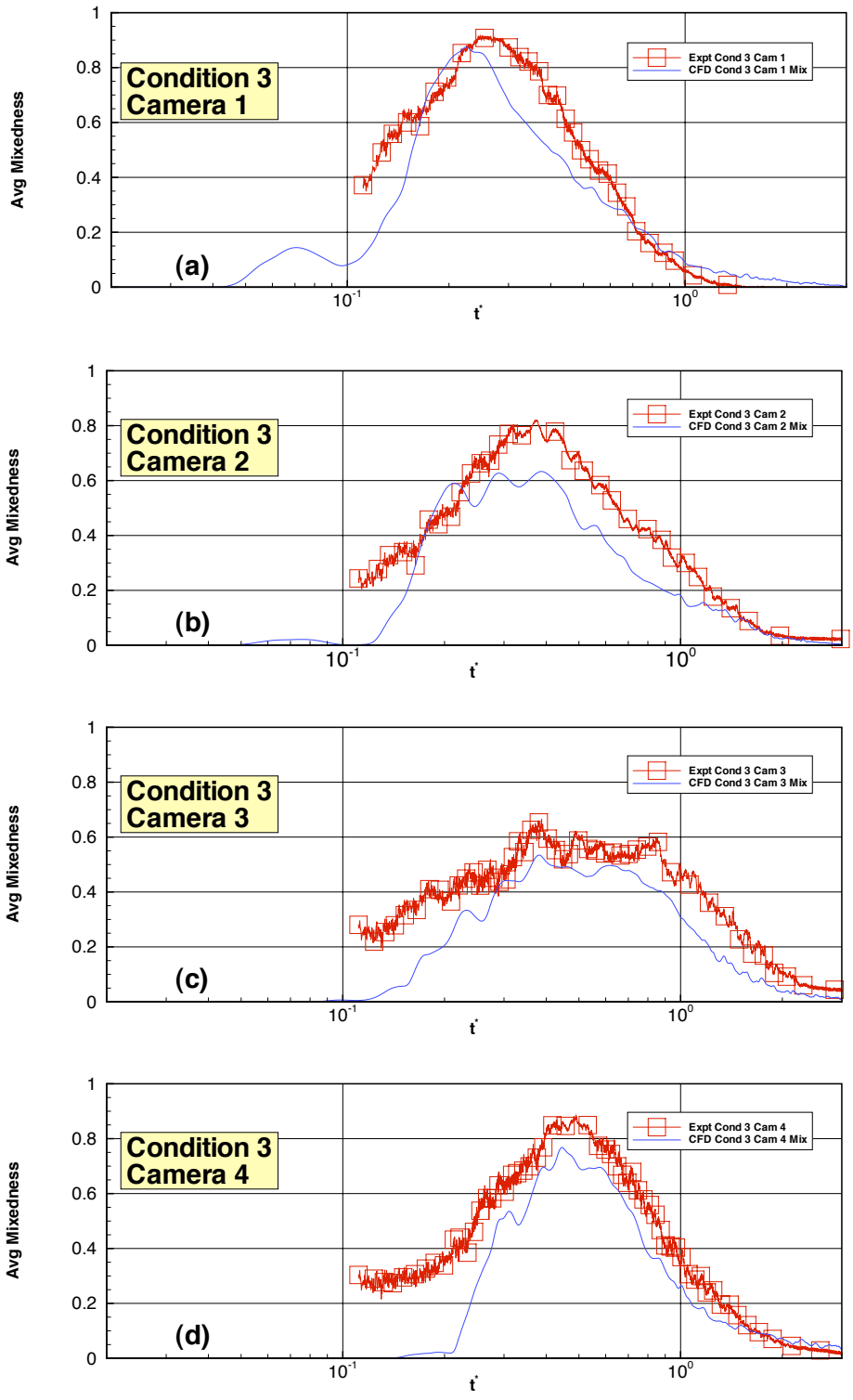

Figure 30. Area-averaged experimental and CFD mixedness time histories for Condition 3; (a) Camera 1 (b) Camera 2 (c) Camera 3 and (d) Camera 4.

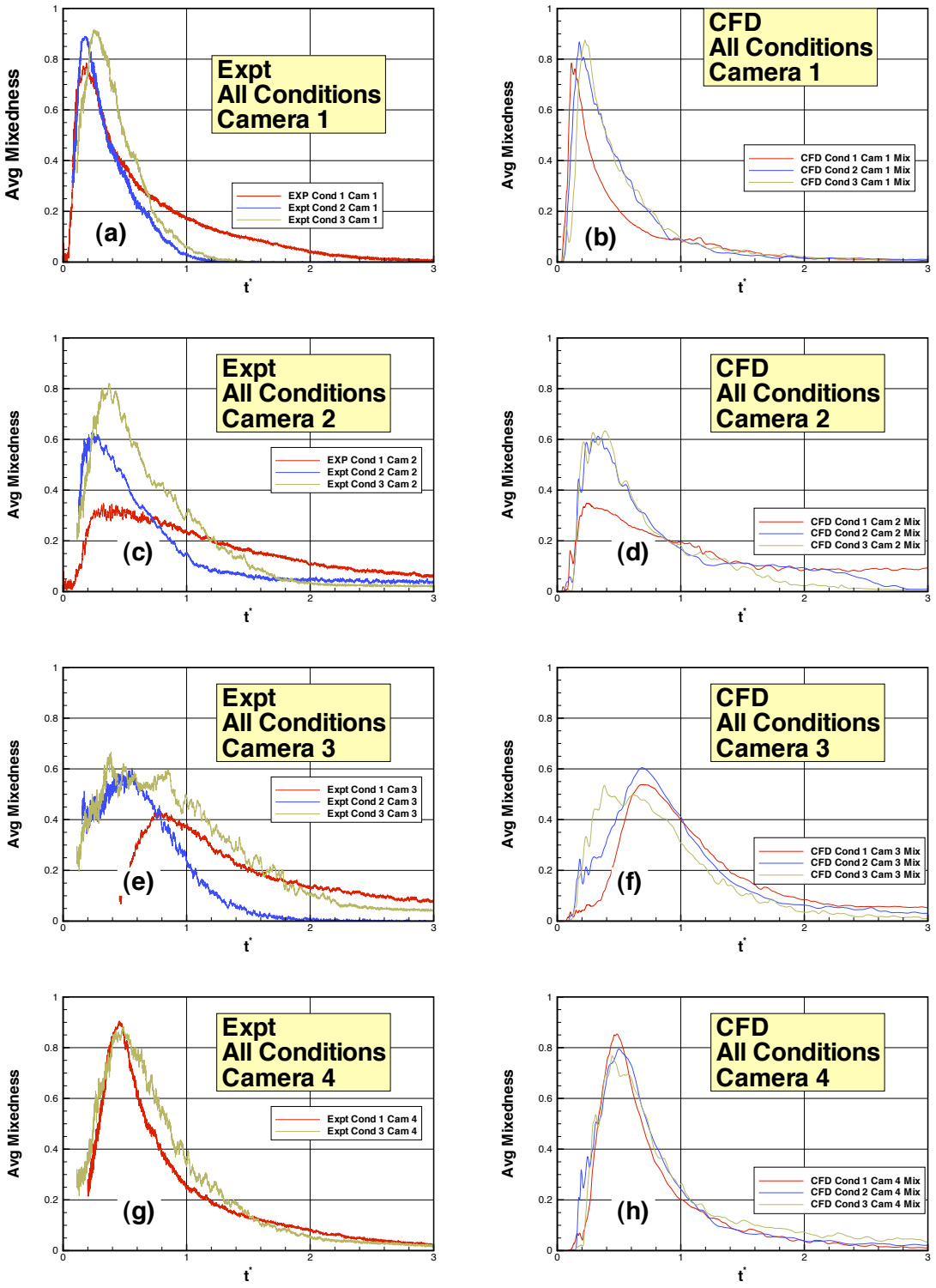

Figure 31. Area-averaged experimental and CFD mixedness (ordinate) time histories for all conditions.

decrease in density difference. The CFD and experiment are remarkably well matched with regards to the peak height. However, later in the exchange, the experiment result for condition 1 exhibits a long tail that reflects higher average mixedness (more mixing) than conditions 2 and 3. This is an anomaly in the measurements because after $t^* = 1$, the flow is highly stratified for both the conditions 2 and 3, which should result in less mixing than condition 1. The CFD data show what should be the correct physical trend.

For Camera 2, the experimental data show that there is a dramatic increase in peak height between Conditions 1, 2 and 3, which seems to be physically correct because of the increase in mixing in the inlet bay, due first to the decrease in density difference (between conditions 1 and 2) and then the increase in flow rate (between conditions 2 and 3). On the other hand, the CFD results show only an increase between Conditions 1 and 2/3 with Conditions 2 and 3 having almost the same peak magnitude. In this case the CFD is probably under-predicting the amount of mixing associated with an increase in flow rate (condition 3).

For Camera 3, the experiment shows that the peak value of mixedness occurs first for condition 3, then 2 and then 1. The CFD has a similar trend. The peak values for CFD and experiments compare well for condition 2. The CFD predicts a higher peak value for condition 1 and a slightly lower peak value for condition 3 compared with experiments. CFD results for Camera 4 compare very well with the experiments, indicating that the CFD correctly captures the mixing due to the impingement of a jet into the rounded side of the tank.

Discussion Regarding Comparison of CFD Predictions to Experimental Results

The ultimate objective of this multi-phase project is to develop a computational tool for predicting whether a given tank design is likely to meet exchange requirements (e.g., predict whether or not it will have 95% EE after 3 TVE). It is shown that the predicted EE match the expected physical trends: as mixing increases, due to either an increase in flow rate or decrease in density difference, the EE at the end of three tank volumes increases (see Figure 21). The computational predictions fall within the 95% uncertainty intervals for the EE computed from experimental data. The EE is an integral measure of the volume of the two fluids within the tank at a given time and therefore is a reflection of the volume of each of the two fluids that exit the tank.

Detailed two-fluid data in four data planes in the physical ballast tank model were collected to obtain a basic understanding of the mixing that occurs in the tank. Here, the experimental uncertainty is much less than it is for EE and it is possible to assess the accuracy with which the CFD model predicts the movement of two fluids throughout the tank and two-fluid mixing. The comparisons show that the CFD can predict the volume fraction quite well implying that the mass movement of the two fluids throughout the tank is well-predicted. The CFD comparisons of mixedness are on the whole, quite good, particularly for the conditions 1 and 2, which involve less mixing. For condition 3, the mixing is under-predicted, particularly due to the mixing in the bellmouth bay.

This type of mixing is highly energetic due to overturning gravity waves and turbulence. Under-prediction of early-stage mixing, especially during the first TVE, will result in less SWVF in the mixture carried to the exit and a greater VF of freshwater being pushed out of the exit. The end result would be slightly higher EE during the first tank volume.

That the EE is higher for the increased mixing conditions 2 and 3 is primarily due to the scouring of freshwater trapped in the tank tops. Small, quarter-round vent holes that are included in the upper corners of the actual tank top structure have not been included in either the experiment tank or CFD model. Undoubtedly, they will contribute to increased EE, but their significance is unknown at this time. One of the limitations of the 1/3-scale model program is that the extent of the 1/3-scale tank is only a fraction of a full-scale tank (i.e., a typical bulk carrier tank has ≈ 10 rows of bays, whereas the 1/3-scale model only has two). This has implications for any conclusions drawn from the EE results: since the 1/3-scale tank is limited to two bay lengths, the relative amount of energy available for mixing and scouring in the two adjacent bays is much higher than across the entire full-scale tank. In the full-scale tank, it is hypothesized that far downstream the energy levels approach quiescent and mixing, no matter what the flow rate and density difference, approaches zero. We follow next with results of CFD simulations for the full-size 705 m^3 (186, 250 $gals$) tank that will shed some light on this concern.

FULL-SCALE CFD SIMULATIONS

Full-scale CFD simulations were performed on interconnected ballast tanks from a typical 35, 000 dwt handysize bulk carrier. The tanks, shown in Figure 32 consist of a total of ten rows of interconnected double bottom tank (DBT), hopper side tank (HST), and wing tank (WT) bays. The dimensions of the tanks are listed in Table 7. The WT bays are connected to the HST bays via two 8 in (0.203m) (ID) connection pipes. The incoming fluid is pumped into the DBT via a single inlet bellmouth as shown in Figure 33.

Table 7. Full scale tank dimensions.

Tank	L (m)	B (m)	H (m)	V (m^3)
DBT	27	3.3	1.4	11.5
HT	27	1.9	5.0	17.4
TT	27	5.2	4.7	41.4

There are two exits that were modeled as flush with the tank top (not shown) directly above the two connection pipes to simulate an overflow condition. The tank floor openings and stiffeners were modeled based on tank drawings provided by Fednav International. The total volume of the tank (with longitudinal stringers) is 705 m^3(186, 250$gals$). The inflow rate was 11.4 m^3/min (3000 gpm), meaning that a one tank volume takes

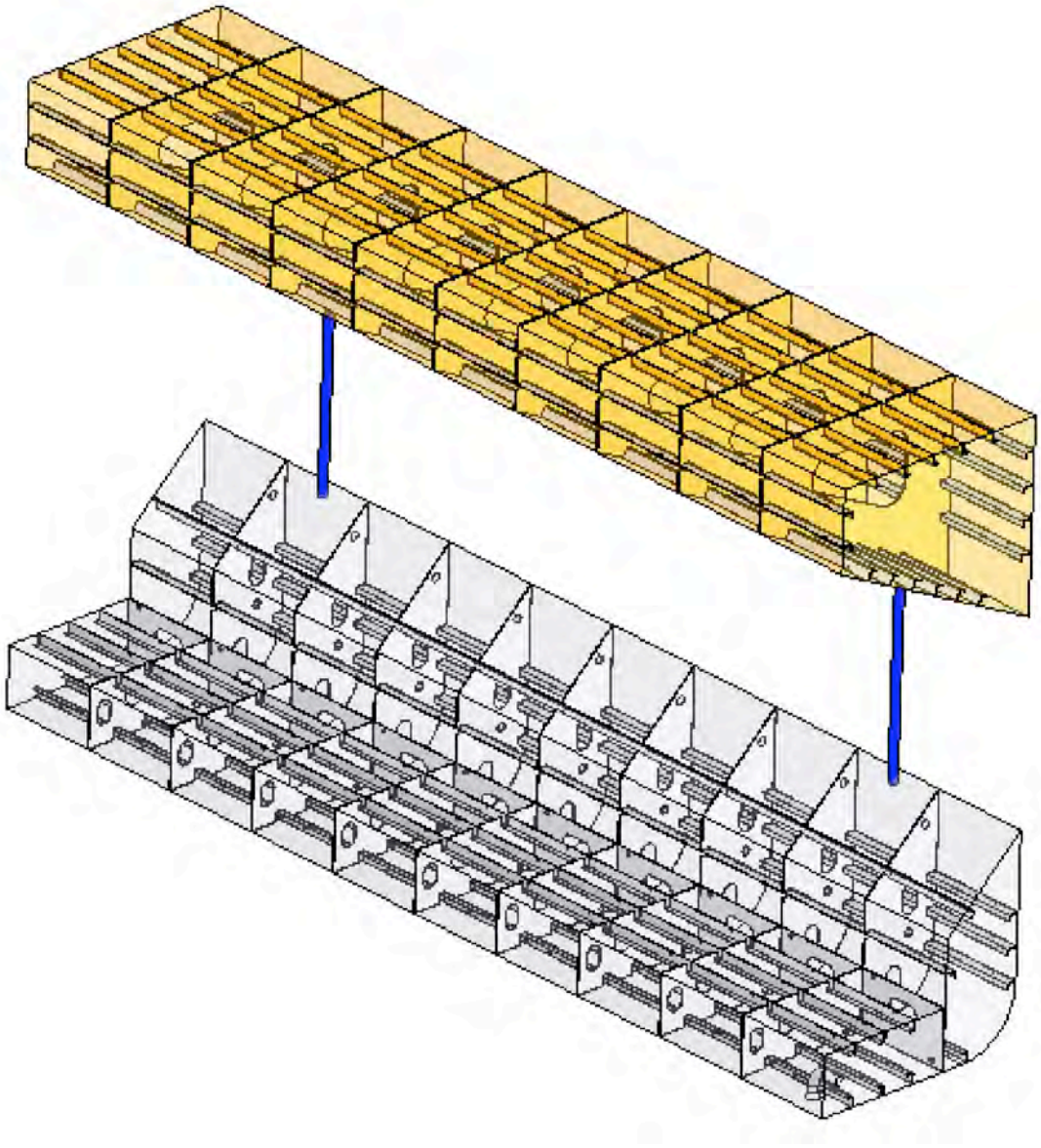

Figure 32. Drawing of bulk carrier tank. Three tanks are shown: lower left: double bottom tank (DBT); lower right: hopper tank (HT) and upper: topside tank (TT).

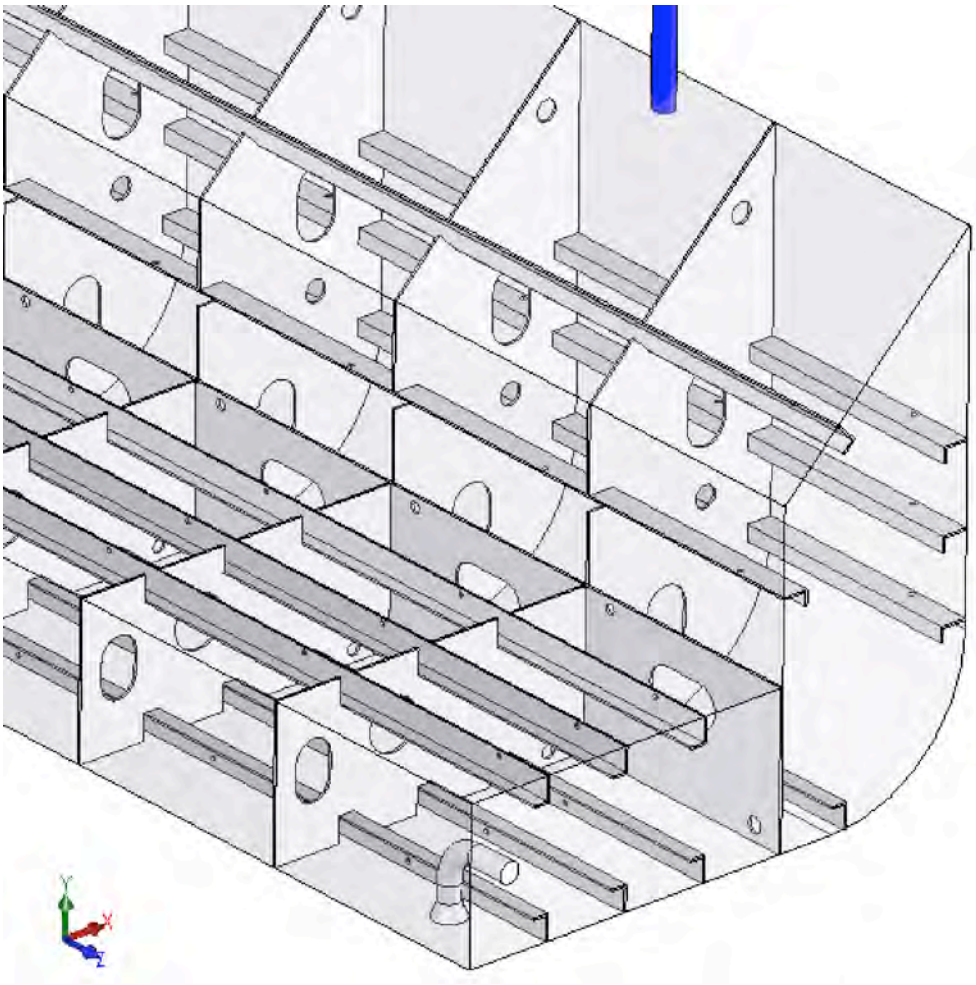

Figure 33. Inlet bay detail for full-scale tank.

62 *min* (physical time). The tank is initially full of freshwater with influent mid-ocean saltwater giving a density difference equivalent to a salinity difference of 35 *ppt*.

In an earlier work, Kent and Parsons[6] concluded that the EE was not affected by the presence of the longitudinal stringers. These structural elements are small in relation to the total tank volume and it is reasonable to assume that they would not affect the EE. Their inclusion imposes a large computational burden meaning that simulations could be performed much quicker without them. In order to investigate the influence of the longitudinal stringers, two separate grids were developed for the full-scale tank, one with all of the tank structure as shown in Figure 32 and one that omits the reinforcing stringers. The grid that did not include the stringers needed approximately 1.3 million cells, while the grid that included the finer structural details required approximately 5.5 million cells. The inclusion of the stringers had a significant impact on the computational resources and time required to perform the simulations as shown in Table 8.

Table 8. Computational details for 1/3-scale and full-scale simulations

	1/3-Scale	FS (no stringers)	FS (with stringers)
Total Volume (m^3)	1.43	711	705
Total Volume ($gals$)	378	187,825	186,250
Total no. Cells	1.3×10^6	1.2×10^6	5.4×10^6
Avg Cell Size (cm)	1.0	8.5	5.0
Platform	NSWCCD		ARL
	banyan	banyan	fcs
No. of cpus	12	12	48
Total Flow Time ($secs$)	1,050	12,000	12,000
No. of Time Steps	3,830	7,300	17,500
Total Wall Time (hr)	51.4	64.2	412

A close-up comparison of the predicted SWEVF very early ($t^* = 0.016$) in the exchange, at several cut planes near the inlet pipe are shown in Figure 34. The figure shows that the stringers cause a large difference in the mixing that takes place. Without stringers the two fluids in the inlet bay are completely mixed, with highly mixed fluid regions thereafter quickly dispersing throughout the tank. With the stringers the flow is much less mixed, with almost pure SW forming overturning waves in the vicinity of the bellmouth and moving along the tank bottom. A series of waterfall flows are occurring, much like in the 1/3-scale tank. The exchange efficiencies for the two cases are shown in Figure 35 as compared with the theoretical lines for perfect mixing and plug flow filling. Perfect mixing occurs if the influent volume fraction in the tank is spatially homogeneous i.e., as the influent enters the tank it is instantaneously mixed. With perfect mixing EE obeys an exponential relationship

$$\eta = 1 - \exp^{-t^*} \tag{7}$$

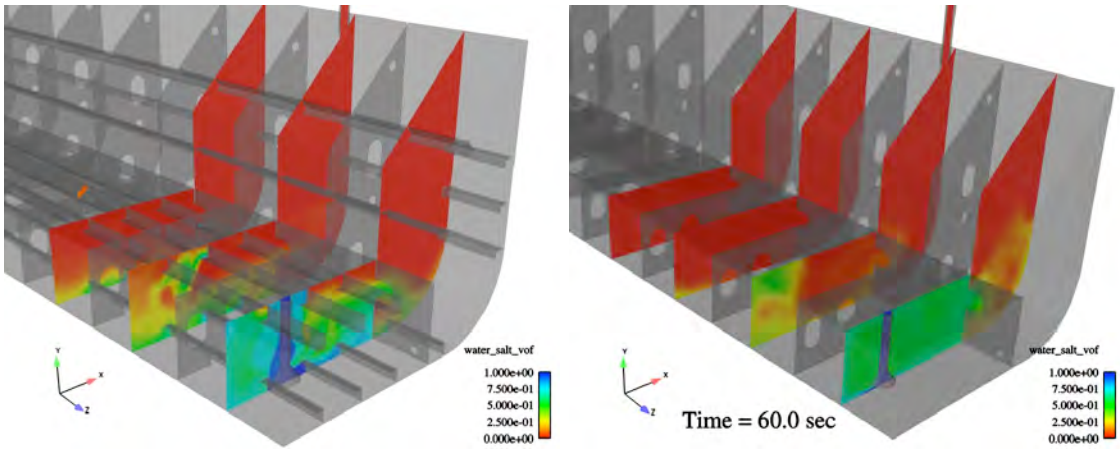

Figure 34. Full-scale SWVF contours at $t^* = 0.016$ ($60secs$); left: with stringers and right: without stringers.

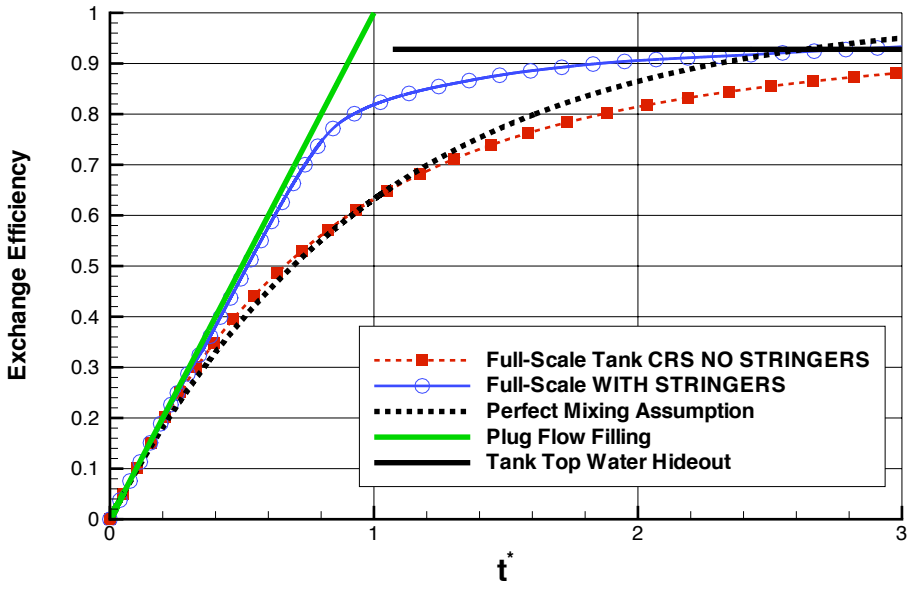

Figure 35. EE time history for full-scale tank showing theoretical perfect mixing and plug flow filling lines.

such that only 95% EE can be obtained after three tank volumes, with 100% not theoretically possible. Plug flow filling occurs when absolutely NO mixing occurs and the influent pushes the original fluid out like a piston. In this case, EE obeys the simple linear relationship

$$\eta = t^* \tag{8}$$

Only a single tank volume is necessary to obtain 100% EE. The horizontal line in Figure 35 is the EE due to water hideout in the tank tops. The theoretical maximum volume of FW that could be trapped by the longitudinal stringers is 7.2% of the total tank volume, giving an EE of 92.8% if all the freshwater except that in the tank tops is flushed from the tank. Figure 35 shows that without stringers the EE curve follows the perfect mixing line, after which it falls off significantly, reaching only 88% EE at t^*=3. On the other hand, the case with stringers follows the plug flow filling line until about t^*=0.8, after which it falls off rapidly, reaching the hideout line (93% EE) at t^*=2.6. This implies that the FW trapped in the tank tops is only partially scoured. The explanation for the drastically different behavior in the EE early on in the exchange is due to the fact that the stringers localize the most energetic mixing from the bellmouth and limit the transverse spread to the width of the stringer spacing. This limits the extent of mixing that takes place and the SW water remains in the bottom of the tank while advecting through the tank in a series of buoyant flow events. The EE curve is linear because only the FW is exiting the tank. On the other hand, in the no stringer case, the SW from the bellmouth is allowed to spread and mix transversely, as well as longitudinally, which, apparently leads to near-perfect mixing in the inlet bay. The mixed region quickly advects throughout the entire tank, carrying SW out the exit. If the influent SW is exiting the tank, the rate of EE increase, i.e., the accumulation of SW in the tank, is reduced.

Table 9 lists the EE values at integer values of $t^*$for the stringer and no stringer cases, as well as the two theoretical curves. From the table it can be seen that in both cases, the EE does not reach the mandated 95% level at t^*=3. The table emphasizes the fact that if plug flow can be achieved 100% EE can be obtained at t^*=1.

Table 9. Exchange efficiencies (full-scale), calculated from CFD simulation data.

t^*	Exchange Efficiency			
	Plug flow	Perfect mixing	w/ stringers	w/o stringers
1	1	0.63	0.82	0.63
2	1	0.86	0.91	0.81
3	1	0.95	0.93	0.88

Figure 36 is a plot of the SWEVF for the full-scale CFD simulations with the theoretical curves for plug flow and perfect mixing. Note that SWEVF from two exits is shown with outlet 1 being at the top of a bay close to the inlet and outlet 2 being the one at the far end of the tank (see Figure 32). Figure 36 shows that, as compared with the

perfect mixing case, the no stringer case has a time lag before any SW mixture reaches either of the outlets. The SWEVF then increases rapidly due to the transport of highly mixed fluid from the inlet bay. The rate of SWEVF increase flattens out and eventually converges with the perfect mixing case. The case with stringers is more similar to the plug flow filling curve, with (except for a small spike early on, explained below) a much longer time before appreciable amounts of SW reach the exits. Surprisingly, the SWEVF in both the outlets act in tandem implying that the mixed water moves first through the double bottom and hopper side tanks, before being transported into the upper wing tank and outlets. This is because the stringers guide the SW to move longitudinally across the tank more easily than transversely in the early stages of BWE.

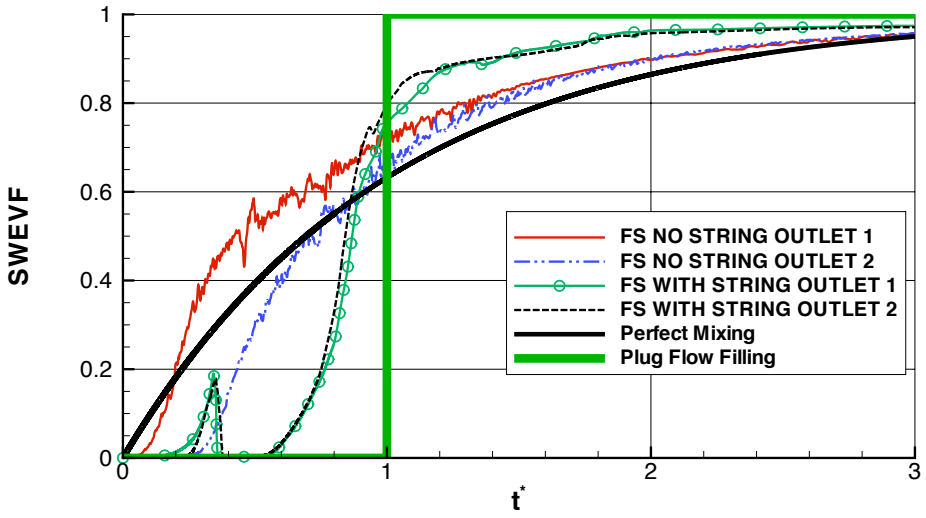

Figure 36. SWEVF time history for full-scale simulations showing theoretical perfect mixing and plug flow filling curves.

The small spike in the SWEVF at around $t^* = 0.3$ is due to the mixing event that occurs at the start of the exchange procedure, as the incoming saltwater mixes with the freshwater in the inlet bay. After this initial mixing event, the mixed fluid is then transported downstream ahead of the bulk fluid motion. Later in the exchange there is significant mixing that occurs as larger amounts of the incoming fluid passes up through the vertical connection pipes and mixes with the fluid in the upper wing bays. As the amount of incoming fluid passing through the connection pipes increases, the effluent concentration profile reflects the large increase in the amount of incoming fluid that is exiting the tank (around 1 TVE).

Discussion of Full-Scale Results

These simulations (Figure 35 and Table 9) indicate that the ballast tank configuration used in bulk carriers may not reach the required 95% EE, however, we cannot say

that at 3 TVE the EE is statistically different than 95%. It appears that the primary cause for loss of EE is trappage of water in the tank tops. The case with stringers approaches 93% EE, which is the limit if water above the level of the tank top structures (overhead longitudinal stringers) remains trapped. The case without stringers is about 5% lower. In these calculations the quarter-round vent holes in the tops of the structure were not included. Since they would allow for some movement of the trapped water along the top of the tank, their addition in the model would probably increase the calculated EE somewhat, though to what extent remains to be seen. The addition of longitudinal stringers to the computational geometry has a profound impact on the two-fluid mixing in the tank and the EE. It is believed that the most important change is in the stringers ability to restrain mixing in the transverse direction. With this limitation, the amount of mixing is dramatically reduced and the SWEVF and EE time histories approach that for plug flow filling. These results would seem to contradict the findings of Kent and Parsons,[6] who performed similar CFD calculations of BWE and concluded that the finer structural details, such as stringers, could be neglected and still achieve sufficiently accurate predictions of the EE. Their study, however, was performed with limited computational resources. The predictions of the J-type bottom/side ballast tank, which is a similar tank arrangement to the geometry used in this study, were performed using only 276,000 cells. The assessment of the impact of the finer structural details was not performed on representative overall tank geometry. Instead, their simulations that included the stringers simply focused on a region of only the double bottom tank bays, which would not account for the mixing that occurs in the hopper tank and topside tank sections where the vertical separations between the structures is also important.

SUMMARY AND CONCLUSIONS

BWE experiments on a 1/3-scale section of a ballast water tank and CFD model simulations for both the 1/3-scale tank and a full-scale ballast tank were performed for three tank volumes of exchange flow. Experiments were conducted under three different conditions: Condition 1: SW flow-through exchange with FW at 4.2 m^3/min (1100 gpm); Condition 2: SW flow-through exchange with brackish water at 4.2 m^3/min (1100 gpm); and Condition 3: SW flow-through exchange with brackish water at 6.4 m^3/min (1700 gpm). A wealth of qualitative and quantitative data were collected from areas of important mixing events within the tank, as well as from the exit pipe, and used to validate the CFD model. These data are also very valuable for understanding the two-fluid flows that occur during BWE. Model scale computations and simulations were performed for the three conditions. The combined experimental and computational approaches have given us new insights into the physics of BWE. Significant findings are:

1. The predicted values of EE fall within the experimental error bands, showing that the CFD model has been validated.

2. Comparisons between CFD and experimental SWEVF and mixedness data within the tank show that the CFD predicts these quantities reasonably well. One shortcoming is the under-prediction of the amount of mixing for condition 3.

3. Neither the CFD nor the experimental model included the quarter-round vent holes that are at the top of the tank bays. These would allow a small flow of the water across the tank top toward the exit pipes, and should act to decrease the water hideout and therefore possibly increase the calculated EE. However, due to size of a full-scale tank, the kinetic energy at the interface and the pressure forces pushing the flow through these holes would be very small.

4. Longitudinal stiffeners (LS) are very effective at decreasing the extent of mixing within the inlet bay. With LS the early exchange approaches plug flow filling. The latter stages of exchange approach the perfect mixing case, but the maximum EE is reduced by FW hideout in the tank top. This result shows that in a full-scale tank there is insufficient kinetic energy to scour water trapped at the tank top (water hideout).

5. Not including the LS in the CFD model allows nearly homogenous and instantaneous mixing to occur across the entire inlet bay. The EE curve approaches that for perfect mixing and is lower than the case including LS.

6. These simulations indicate that if mixing in the inlet bay can be substantially reduced, AND the quarter-rounds at the tank tops are effective in reducing the water hideout in the tank tops, it may be possible to perform a 95% exchange in significantly less than 3 TVs.

CFD allows examination of a wide range of ballast exchange conditions across any tank architecture. It allows evaluation of the effects of various parameters and small-scale tank architecture on the outcomes of exchange. One aspect of ballast water exchange not incorporated into the present model is the effects of ship motion on the exchange process – ballast water exchange must be conducted on the high seas. Additional work on this application of CFD modeling should incorporate equations of motion that account for roll and pitch of a moving vessel. We conclude that CFD modeling is a very useful approach to understand ballast tank flow and that use of CFD model-based calculations of EE can be a practical alternative to on-board experiments. However, appropriate resolution of tank structure and CFD cell grid densities must be allowed for maximum benefit.

APPENDIX A: UNCERTAINTY ANALYSIS

LIF Measurements

Mixedness and Volume of Fluid Measurements

The mixedness at a point (x, y) is given by the following equations:

$$N(x,y) = \begin{cases} > S & : \quad M(x,y) = 0 \\ \geq \frac{S}{2} & : \quad M(x,y) = \frac{1}{2}\left[S - N(x,y)\right] \\ < \frac{S}{2} & : \quad M(x,y) = \frac{1}{2}\left[N(x,y)\right] \end{cases} \tag{9}$$

where the normalized intensity $N(x, y)$ is given by:

$$N(x,y) = S\frac{I(x,y) - DF(x,y)}{BF(x,y) - DF(x,y)} \tag{10}$$

The mixedness is proportional to the quantity $N(x, y)$. If the parameters$\Delta\ I_d$ and$\Delta\ I_c$ and their associated uncertainties are defined as follows:

$$\Delta I_d = I(x,y) - DF(x,y) \tag{11}$$
$$\Delta I_c = BF(x,y) - DF(x,y) \tag{12}$$
$$U_{\Delta I_d} = U_I + U_{DF} \tag{13}$$
$$U_{\Delta I_c} = U_{BF} + U_{DF} \tag{14}$$
$$\tag{15}$$

The normalized intensity $N(x, y)$ now becomes:

$$N(x,y) = S\frac{\Delta I_d}{\Delta I_c} \tag{16}$$

The uncertainty in N is governed by the following equation:

$$\left(\frac{U_N}{N}\right)^2 = \left(\frac{S}{N}\frac{\delta S}{\delta N}\right)^2\left(\frac{U_S}{S}\right)^2 + \left(\frac{\Delta I_d}{N}\frac{\delta N}{\delta \Delta I_d}\right)^2\left(\frac{U_{\Delta I_d}}{\Delta I_d}\right)^2 + \left(\frac{\Delta I_c}{N}\frac{\delta N}{\delta \Delta I_c}\right)^2\left(\frac{U_{\Delta I_c}}{\Delta I_c}\right)^2 \tag{17}$$

Since S is a constant scaling factor, the first term on the right hand side of the above equation vanishes. Using the equations for the uncertainties in$\Delta\ I_d$ and$\Delta\ I_c$, the uncertainty in N becomes:

$$\left(\frac{U_N}{N}\right)^2 = \frac{U_I^2 + U_{DF}^2}{\Delta I_d^2} + \frac{U_{BF}^2 + U_{DF}^2}{\Delta I_c^2} \tag{18}$$

Since $M(x, y)$ is a function of the constant S and $\frac{1}{2}N(x, y)$, the relative uncertainty in $M(x, y)$ is given by the following equation:

$$\left(\frac{U_M}{M}\right)^2 = \left(\frac{U_N}{N}\right)^2 = \frac{U_I^2 + U_{DF}^2}{\Delta I_d^2} + \frac{U_{BF}^2 + U_{DF}^2}{\Delta I_c^2} \tag{19}$$

Since the volume of fluid is directly related to the quantity $N(x, y)$, the relative uncertainty in the volume of fluid measurement at each point can be written as:

$$\left(\frac{U_{VOF}}{VOF}\right)^2 = \left(\frac{U_N}{N}\right)^2 = \frac{U_I^2 + U_{DF}^2}{\Delta I_d^2} + \frac{U_{BF}^2 + U_{DF}^2}{\Delta I_c^2} \tag{20}$$

Therefore, the relative uncertainty of the volume of fluid measurement is identical to the relative uncertainty of the mixedness. The uncertainties in the data, bright field, and dark field intensities can be expressed in the form:

$$U_I^2 = B_I^2 + P_I^2 = B_I^2 + 2S_I^2 \tag{21}$$
$$U_{BF}^2 = B_{BF}^2 + P_{BF}^2 = B_{BF}^2 + 2S_{BF}^2 \tag{22}$$
$$U_{DF}^2 = B_{DF}^2 + P_{DF}^2 = B_{DF}^2 + 2S_{DF}^2 \tag{23}$$
$$\tag{24}$$

The bias (or systematic) error in the intensity measurements depend on several factors, including the response time of the fluorescent dye, the repeatability of the laser intensity from frame to frame, and the pixel discretization of the intensity by the CCD cameras. The intensity measured by a pixel in the CCD camera can be estimated by the following equation, where I_p is the measured intensity, ϵ is the fluorescence efficiency of the dye, L is the light emitted by the laser source,$\Delta\ t$ is the exposure time of the camera, and A is the area of the measured area:

$$I_p \propto D\left(\frac{\epsilon L \Delta t}{A}\right) \tag{25}$$

Therefore, bias uncertainty of the measured intensity I_p can be expressed as:

$$B_{IP}^2 = B_\epsilon^2 + B_L^2 + B_{\Delta t}^2 + B_A^2 + B_D^2 \tag{26}$$

The dye response time is considered in this work to have little effect on the uncertainty in the intensity measurement, since the camera exposure time is much greater than the response time of the dye molecules. In addition, the dye efficiency is assumed in this work to be constant throughout the fluid medium. Therefore, the term B_ϵ vanishes in the above equation. This assumption is supported by the fact that the variation in the laser light dominates the collected intensity. In addition, characterizing the stability of the collected light will also include effects from dye performance. This work also assumes that the errors due to CCD leakage are small since the intensities collected were well below saturation values for the CCD sensors, and that the error in the measured area is extremely small since the optics used do not move with respect to the target plane. Therefore, the term B_A disappears and the only remaining significant terms are those originating from laser intensity, discretization error, and camera exposure time. The repeatability of the laser intensity was measured using the bright field images. The average intensity in the measurement region was calculated for each frame taken during a bright field run, and the standard deviation of the measured average intensity was used as the laser intensity uncertainty. For pixel discretization, an uncertainty of one pixel

was used as the uncertainty in intensity. The bias errors resulting from each systematic source are listed in Table 10. As shown in Table 10, the uncertainty in the exposure time is extremely small in comparison to the variations in laser illumination, and the bias error on a single pixel basis is approximately 2.73%. The random uncertainty of the

Table 10. Bias error sources for measured intensity for a single pixel.

Error Source	B_L (counts)	B_D (counts)	$B_{\Delta t}(sec)$	B_{IP} (counts)
Absolute Value	1.1755	1	0.1×10^{-6}	1.5433
Relative	0.0046	0.003922	1.5×10^{-6}	0.00605

bright field and dark field images was calculated by sampling single pixels in the bright and dark field run and calculating the standard deviation of the measured intensity. For the intensity during data collection, pixel histories in the images at full concentration at the beginning of an experimental run were analyzed in order to quantify the random error in the measured intensity during a run to include the effects of moving fluid. The bias errors PDF, PBF, and PI are listed in Table 11. The values listed in Table 11 are

Table 11. Bias error sources for measured intensity for a single pixel.

Quantity	DF	BF	I
Mean Value (counts)	4.6217	50.669	37.6473
Relative Random Error	0.4601	0.0661	0.0802

on a pixel by pixel basis. The mixedness and volume of fluid measurements reported in this work represent an average over the interrogation area. Therefore, in order to characterize the measurement uncertainty properly, the uncertainty of the measurement must be calculated for each camera. Using the calculated values and equations above, the calculated relative uncertainties for each interrogation region are listed in Table 6. The single point random uncertainty P_M is used to calculate $P_{\bar{M}}$ based on the number of points in the corresponding interrogation region. Based on this uncertainty analysis, the relative uncertainty in the LIF measurements of mixedness and volume of fluid are approximately 0.66% over the whole field, while for a single pixel measurement the relative uncertainty approaches 9.84%. Therefore, the LIF measurement of mixedness and volume of fluid over an entire bay has a very low uncertainty due to the large number of points interrogated simultaneously. It should be noted that in future studies the linearity of the CCD sensor response versus dye concentration will be performed experimentally in order to better estimate the error associated with the assumption of linear response.

Table 12. Relative uncertainties for LIF measurement regions.

Quantity	B_M	P_M	No. of pts.	$P_{\bar{M}}$	$\frac{U_M}{M}$	$\frac{U_{VOF}}{VOF}$
Cam 1	0.006614	0.09815	1388400	8.330E-05	0.006615	0.006615
Cam 2	0.006614	0.09815	1325768	8.524E-05	0.006615	0.006615
Cam 3	0.006614	0.09815	1429785	8.208E-05	0.006615	0.006615
Cam 4	0.006614	0.09815	1299047	8.612E-05	0.006615	0.006615

REFERENCES

1. Ballast water management convention. Technical report, International Maritime Organization, 2005.

2. Ballast water treatment technology: current status. Technical report, Lloyds Register, 2007.

3. P. Atsavapranee and M. Gharib. Structures in stratified plane mixing layers and the effects of cross-shear. *Journal of Fluid Mechanics*, 342:53–86, 1997.

4. Peter Chang, Wesley Wilson, Stephan Verosto, and Paisan Atsavapranee. Assessment of the refueling performance of ddg 51 compensated fuel/ballast tanks. In *ASNE Fleet Maintenance Symposium*, San Diego, CA, 2001. San Diego Section of the American Society of Naval Engineers.

5. A.E. Holdo, G. A. Armstrong, and A. Rose. An analysis of flow-through ballast water exchange. In *International Conference on Marine Engineering Systems/The Society of Naval Architects and Marine Engineers (8th ICMES/SNAME)*, pages A6–1–A6–10, New York, NY, 2000.

6. Christopher P. Kent and Michael G. Parsons. Computational fluid dynamics study of the effectiveness of flow-through ballast exchange. *Transactions of the SNAME*, 112, 2004.

7. G. Rigby and G. Hallegraeff. The transfer and control of harmful marine organisms in shipping ballast water: behaviour of marine plankton and ballast water exchange trials on the mv iron whyalla. *J. of Marine Env. Eng'g*, 1:91–110, 1994.

8. G. M. Ruiz and David F. Reid. Current state of understanding about the effectiveness of ballast water exchange (bwe) in reducing aquatic nonindigenous species (ans) introductions to the great lakes basin and chesapeake bay, usa: Synthesis and analysis of existing information. Technical Report GLERL-142, NOAA, 2007.

9. Wesley Wilson, Peter A. Chang, Stephan Verosto, Paisan Atsavapranee, David Reid, and Phil Jenkins. Computational and experimental analysis of ballast water exchange. In *Maritime Environmental Engineering Symposium (MEETS 2006)*, Crystal City, VA, 2006. ASNE.